Volcano Seismology

BERNARD CHOUET[1]

Abstract — A fundamental goal of volcano seismology is to understand active magmatic systems, to characterize the configuration of such systems, and to determine the extent and evolution of source regions of magmatic energy. Such understanding is critical to our assessment of eruptive behavior and its hazardous impacts. With the emergence of portable broadband seismic instrumentation, availability of digital networks with wide dynamic range, and development of new powerful analysis techniques, rapid progress is being made toward a synthesis of high-quality seismic data to develop a coherent model of eruption mechanics. Examples of recent advances are: (1) high-resolution tomography to image subsurface volcanic structures at scales of a few hundred meters; (2) use of small-aperture seismic antennas to map the spatio-temporal properties of long-period (LP) seismicity; (3) moment tensor inversions of very-long-period (VLP) data to derive the source geometry and mass-transport budget of magmatic fluids; (4) spectral analyses of LP events to determine the acoustic properties of magmatic and associated hydrothermal fluids; and (5) experimental modeling of the source dynamics of volcanic tremor. These promising advances provide new insights into the mechanical properties of volcanic fluids and subvolcanic mass-transport dynamics. As new seismic methods refine our understanding of seismic sources, and geochemical methods better constrain mass balance and magma behavior, we face new challenges in elucidating the physico-chemical processes that cause volcanic unrest and its seismic and gas-discharge manifestations. Much work remains to be done toward a synthesis of seismological, geochemical, and petrological observations into an integrated model of volcanic behavior. Future important goals must include: (1) interpreting the key types of magma movement, degassing and boiling events that produce characteristic seismic phenomena; (2) characterizing multiphase fluids in subvolcanic regimes and determining their physical and chemical properties; and (3) quantitatively understanding multiphase fluid flow behavior under dynamic volcanic conditions. To realize these goals, not only must we learn how to translate seismic observations into quantitative information about fluid dynamics, but we also must determine the underlying physics that governs vesiculation, fragmentation, and the collapse of bubble-rich suspensions to form separate melt and vapor. Refined understanding of such processes—essential for quantitative short-term eruption forecasts—will require multidisciplinary research involving detailed field measurements, laboratory experiments, and numerical modeling.

Key words: Long-period events, fluid-filled crack model, hydrothermal systems, magmatic transport, high-resolution tomography, very-long-period seismicity, laboratory experiments with analog fluids, Q, Sompi method.

[1] U. S. Geological Survey, 345 Middlefield Road, MS 910, Menlo Park, California 94025, U.S.A. E-mail: chouet@chouet.wr.usgs.gov

Introduction

A central goal of volcano seismology is to understand the nature and dynamics of seismic sources associated with the injection and transport of magma and related hydrothermal fluids. Its ultimate objective is the elaboration of a comprehensive theory of seismic sources associated with volcanic activity that can be applied to a quantitative interpretation of elastic wavefields associated with magmatic and/or hydrothermal transport in volcanoes. To reach these objectives, volcano seismologists must tackle wave emission and radiation problems in both elastodynamics and mutiphase-fluid dynamics.

The course of volcano seismology was fundamentally altered in the late 1970s with the publication of a landmark paper by AKI *et al.* (1977a) and companion papers by AKI and LEE (1976), AKI *et al.* (1976), HUSEBYE *et al.* (1976), and AKI (1977), in which Aki and his colleagues developed a method for the determination of the three-dimensional seismic structure of the lithosphere based on an inversion of earthquake travel-time data. Tomography techniques have since become the most diagnostic approaches to image complex heterogeneous volcanic structures and detect and map magma reservoirs.

In another breakthrough, AKI *et al.* (1977b) used the standard elastodynamics theory to develop a seminal model of the dynamics of a fluid-driven crack, which for the first time provided a quantitative basis for the study of the source of volcanic tremor and long-period (LP) events. A few years later, AKI and KOYANAGI (1981) published a study of the kinematics of magma injection and ascent beneath Kilauea Volcano, Hawaii, which provided a quantitative estimate of the magma transport budget beneath this volcano based on seismic observations. Another study by AKI (1984) discussed magmatic activity beneath Long Valley Caldera, California, and proposed a quantitative basis for an estimation of the energetics of volcanic tremor.

Concurrently with these theoretical advances, AKI *et al.* (1978) conducted a series of key field experiments at Kilauea Iki, Hawaii, in which they demonstrated that the use of multiple seismic methods is essential for a determination of a complex seismic structure such as found in a cooling, partially solidified basaltic lava lake (RICHTER and MOORE, 1966; RICHTER *et al.*, 1970; HELZ, 1993; BARTH *et al.*, 1994). In active and passive experiments conducted at Kilauea Iki, Aki and associates used a combination of *P* waves and surface waves from explosions detonated in the lake crust to determine the velocity structure of the lava lake, relied on teleseismic *S* waves transmitted through the residual lens of melt to further constrain the shear velocity structure, and obtained an estimate of the lateral dimensions of the still-molten magma lens from the spatial distribution of seismic events originating within the cooling crust.

These early efforts, along with parallel studies inspired by Aki's work (FEHLER and AKI, 1978; CHOUET, 1979, 1981, 1982, 1985; FEHLER and CHOUET, 1982; FEHLER, 1983), established a sound physical basis for the interpretation of volcanic

phenomena and provided the impetus that transformed volcano seismology from a qualitative into an increasingly quantitative science. As quantitative volcano seismology ushered in a new era in our understanding of volcanic processes and structures, concurrent technological developments occurred that further advanced the field. With the emergence of portable broadband seismic instrumentation, availability of digital networks with wide dynamic range, and development of new powerful analysis techniques made possible by greatly increased computer capacity, volcano seismology has now reached a mature stage where insights are rapidly being gained on the role played by magmatic and hydrothermal fluids in the generation of seismic waves.

A critically important area of research in volcano seismology today is aimed at the quantification of the source properties of LP events and tremor. The origins of LP events and tremor are critical to understand because this type of seismicity commonly precedes and inevitably accompanies volcanic eruptions and, therefore, can be used to assess the eruptive state or near-term eruptive potential of a volcano (CHOUET et al., 1994; CHOUET, 1996a). Monitoring of precursory seismicity at restless volcanoes is the most reliable, diagnostic, and widely used technique in volcano monitoring (SCARPA and TILLING, 1996). Other key areas of research include the elaboration of the three-dimensional velocity structure of volcanic edifices using high-resolution tomography, and imaging of magma conduits and quantification of magma transport from very-long-period (VLP) seismic data (CHOUET, 1996b). High-resolution tomography is critical to studies of source processes in volcanoes, because the precision and accuracy achieved in the identification of forces operating in a volcano depend on the degree of resolution achieved for the volcanic structure. High-resolution tomography based on iterative inversions of seismic travel-time data can image three-dimensional structures at scales of a few hundred meters provided adequate local short-period earthquake data are available. Thus, temporal variations in forces in a volcano are potentially resolvable for periods as short as a few seconds. Knowledge of the distribution of these forces, their amplitudes, and time histories represents the first step toward assessing the fluid-pathway geometry and mass-transport budget in a volcano.

Once the source space-time functions of the forces associated with fluid transport are known, the next step is to interpret these forces in terms of a physically realistic model of the fluid dynamics. A better understanding of the mechanisms driving fluid-induced seismicity can only be obtained from detailed analyses of the dynamic interactions between gas, liquid, and solid. A logical step toward achieving this goal is to rely on observations derived from well-controlled laboratory experiments with fluids with physical properties analogous to those in active volcanic conduits. The different flow regimes and associated characteristic pressure-oscillation behavior observed in expanding gas-liquid flows produced under experimental conditions may then be modeled numerically. If similarities between seismic and laboratory observations can be demonstrated, the resulting models then may be applied to

quantitatively interpret the observed seismic data. Laboratory experiments conducted to date strongly suggest that pressure oscillations are fundamental phenomena resulting from dynamic flow processes involving the gas and liquid phases. The detailed documentation of the behavior of such flows and of their similarities to observed ground responses to flow within volcanic conduits is a prerequisite to translating seismic information into flow processes and modeling these processes. Such laboratory investigations represent another fundamental area of research in volcano seismology that is critical to the interpretation of magmatic and hydrothermal processes.

The present article offers a brief review of the state-of-the-art in volcano seismology and addresses basic issues in the quantitative interpretation of processes operative in active volcanic systems. The article covers volcano structure (via tomography) and the physics and quantitative analysis of source processes for volcanic earthquakes with examples based on work by the author and his colleagues. This discussion is not intented to be a comprehensive review of the entire field, however. Additional perspectives on other aspects of the field may be found in papers by MCNUTT (2000a, 2000b), which focus more on empirical properties of volcanic earthquake swarms and on case histories for some well-known eruptions.

Volcanic Structures Imaged from High-resolution Three-dimensional Travel-time Tomography

The three-dimensional velocity structure of a volcanic edifice can be imaged through the inversion of first-arrival times from local earthquakes. The technique uses crisscrossing ray paths to separate the integrated effects of slowness (the reciprocal of velocity) on travel times and derive an image of the velocity structure. The arrival time of a seismic wave from an earthquake at a receiver is expressed by the nonlinear relationship

$$t = \tau + \int_{\ell[u(\vec{r})]} u(\vec{r})\, d\ell, \tag{1}$$

where t is the arrival time, τ is the earthquake origin time, $u(\vec{r})$ is the slowness, $d\ell$ is the differential length along the ray, and $\ell[u(\vec{r})]$ is the ray path, a function of the earthquake location and velocity structure. Linearization of eq. (1) about a starting reference model and earthquake location then yields the relation (HOLE, 1992; BENZ et al., 1996)

$$r_{ij} = \sum_{k=1}^{3} \frac{\partial T_{ij}}{\partial x_k} \Delta x_k + \Delta \tau_i + \int_{\text{raypath}} \delta u(\vec{r})\, d\ell, \tag{2}$$

where r_{ij} is the arrival time residual for the i-th earthquake and j-th receiver, T_{ij} is the travel time from the i-th earthquake to the j-th receiver, $\partial T_{ij}/\partial x_k$ are the partial

derivatives of travel time with respect to the spatial earthquake coordinates, x_k, Δx_k and $\Delta\tau_i$ are perturbations to the starting earthquake location and origin time, respectively, and $\delta u(\vec{r})$ is the slowness perturbation to the reference model. The arrival time residual is the difference between the observed travel time and calculated travel time based on the starting earthquake location and reference slowness model.

In this approach, the initial reference slowness model is discretized by a uniformly spaced set of grid points in three dimensions; the first arrival times from a source location to each node in the model are calculated using finite-difference operators based on the Eikonal equation assuming a constant slowness within each cell (VIDALE, 1988, 1991; PODVIN and LECOMTE, 1991). Once the travel times are known everywhere in the model for a given source, rays are found by tracing from the receivers back to the source through the travel-time field. The ray within each cell is approximated by a straight segment and the ray direction is taken along the average travel-time gradient across the cell. Once a ray is traced, the length increments $d\ell$ within all cells crossed by the ray are known, and slowness and hypocenter perturbations are calculated by minimizing the differences between observed and calculated travel times. The model is then updated by the addition of the model perturbations, and the resulting new reference model is used for another linearized inversion. Iterations are stopped when the root-mean-square error in travel times between data and model reaches a stable minimum value.

High-resolution velocity models (0.5 km resolution) of the Kilauea caldera region were obtained by DAWSON et al. (1999) by tomographic inversion of P- and S-wave arrival times from local earthquakes. The data used for their inversion were recorded on a network of 67 stations, including 16 permanent vertical-component seismometers from the Hawaiian Volcano Observatory (HVO) short-period network, and 51 temporary three-component seismometers deployed as part of a joint Japan-U.S. seismic experiment (MCNUTT et al., 1997) (Fig. 1). The average receiver spacing within 5 km of the center of the caldera is about 650 m. The data include 4695 P-wave and 3195 S-wave arrivals from 206 earthquakes during a 20-day period from January 15 through February 3, 1996.

Map views of the P-wave velocity and V_P/V_S models are shown for four depths in Figure 2. High P-wave velocities are observed along the southwest and east rift zones and within the northeast and southwest sectors of the caldera in the shallowest 1 km of structure. Low-velocity zones are observed in the first kilometer of structure in the center and along the south edge of the caldera. One kilometer below the surface, a marked low P-wave anomaly with lateral dimensions on the order of the size of the caldera is resolved. This anomaly is centered on the southeastern edge of the caldera and extends 3 km south-southeast of the caldera. The anomaly extends in depth to 4 km below the surface and has a maximum velocity contrast of about 10% with the surrounding region. Using a 5% reduction in velocity contrast from the initial model, the volume of the anomaly is estimated to be approximately 27 km^3. Corresponding V_p/V_s ratios within the first kilometer show high values along the south and
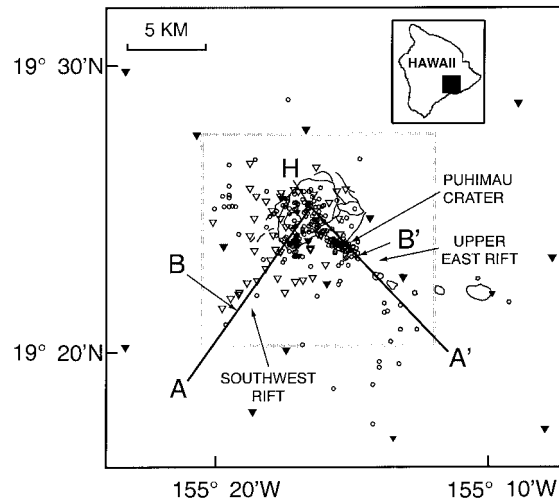
Figure 1

Map of the Kilauea caldera region with inset showing the island of Hawaii and model boundary (black box). The map boundary outlines the horizontal extent of the initial models. The square bounded by dashed, shaded perimeter delimitates the horizontal extent of the *P*-wave velocity model shown in Figures 2a–d and V_P/V_S model shown in Figures 2e–h. Fractures and pit craters are indicated by solid lines. Solid inverted triangles mark vertical-component stations of the HVO permanent network, open triangles indicate temporary three-component stations, and open circles mark earthquake locations. Lines A–A' and B–B' mark the locations of the vertical sections shown in Figures 3a–b. *H*, which marks the apex of these two profiles, is located 1 km northeast of the Halemaumau pit crater. (Modified from DAWSON *et al.*, 1999.)

southeastern outline of the caldera. Below 1 km depth, a high V_p/V_s ratio occupies the same region as the low *P*-wave anomaly, but separates into two distinct zones (Fig. 2g), one centered on the southern portion of the caldera, the other beneath the upper east rift.

Of interest in the shallow (<1 km depth) structure beneath Kilauea are the marked low-velocity zones to the south of the caldera and near the Halemaumau pit crater. The first zone correlates well with the caldera fracture system and a region of thick tephra and ash deposits to the south of the caldera. The second zone within the caldera may be attributed to reduced *P*-wave velocities due to hydrothermal activity at Halemaumau. The high *P*-wave velocities in the southwestern and northeastern portions of the caldera are attributed to accumulated prehistoric and historic pahoehoe flows.

The V_P/V_S model clearly shows that the shear-wave velocity in the upper 5 km beneath the southern portion of the caldera and the upper east rift is anomalously low. The corresponding Poisson ratio in the anomalous region approaches values near 0.37, suggestive of the presence of either highly fractured material and/or a significant fraction of partial melt. Theoretical calculations of seismic wave velocities for different melt geometries (MAVKO, 1980) and constitutive relations of solid-liquid
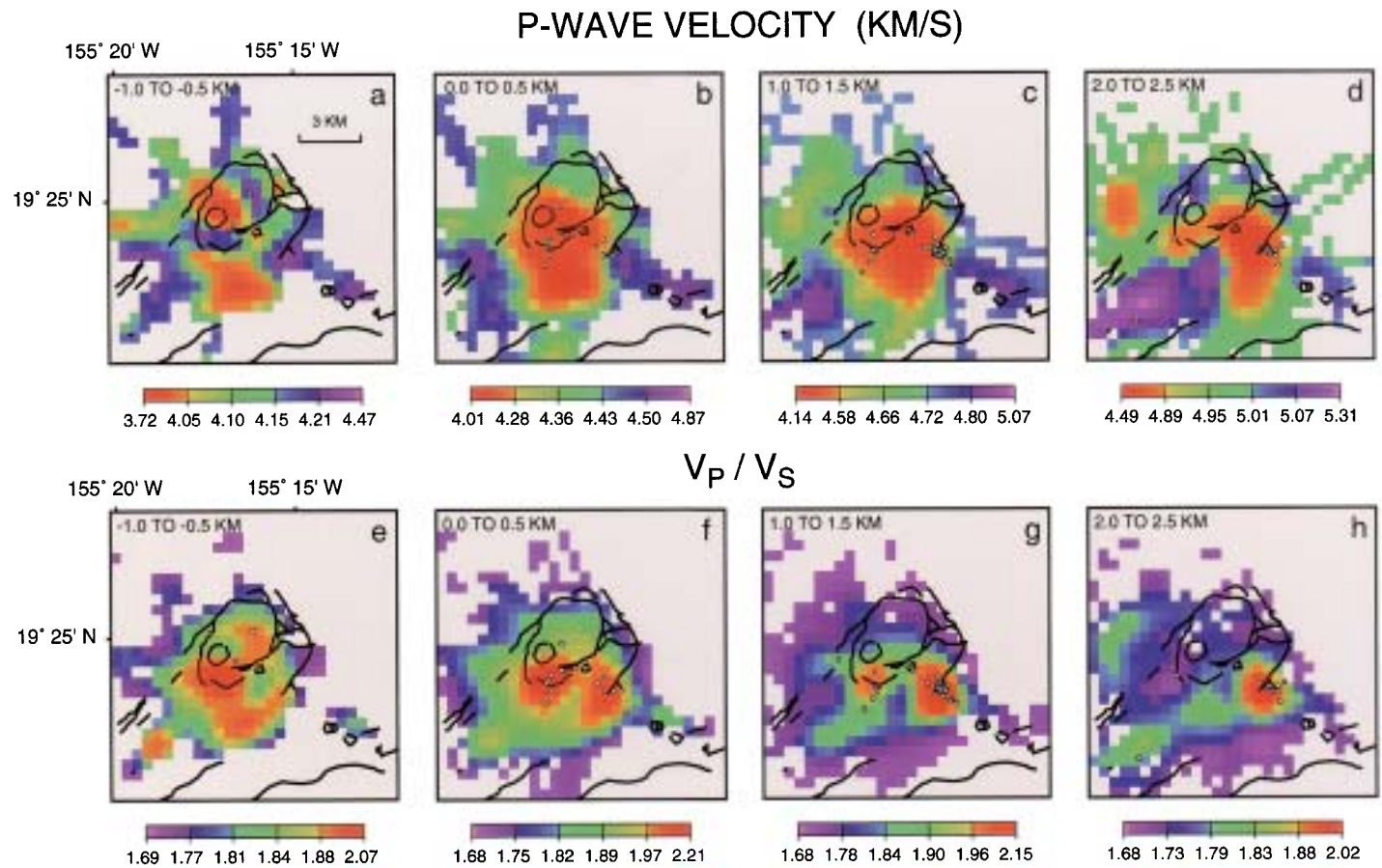
P-WAVE VELOCITY (KM/S)

155° 20' W   155° 15' W

19° 25' N

3 KM

| a | b | c | d |

-1.0 TO -0.5 KM   0.0 TO 0.5 KM   1.0 TO 1.5 KM   2.0 TO 2.5 KM

3.72 4.05 4.10 4.15 4.21 4.47   4.01 4.28 4.36 4.43 4.50 4.87   4.14 4.58 4.66 4.72 4.80 5.07   4.49 4.89 4.95 5.01 5.07 5.31

V_P / V_S

155° 20' W   155° 15' W

19° 25' N

| e | f | g | h |

-1.0 TO -0.5 KM   0.0 TO 0.5 KM   1.0 TO 1.5 KM   2.0 TO 2.5 KM

1.69 1.77 1.81 1.84 1.88 2.07   1.68 1.75 1.82 1.89 1.97 2.21   1.68 1.78 1.84 1.90 1.96 2.15   1.68 1.73 1.79 1.83 1.88 2.02

Figure 2

Map views of the P-wave velocity (a–d) and V_P/V_S velocity ratio (e–h) at four depths. Zero depth indicates sea level and negative depths indicate elevations above sea level. The spatial resolution is 500 m. Pit craters and fractures are indicated by solid black lines. White circles indicate earthquake hypocenters within each layer. (From DAWSON et al., 1999, after correction for erroneous color scales in the original V_P/V_S panels.)

composites (TAKEI, 1998) suggest an approximately 1% perturbation in *P*-wave velocity is equivalent to a 1% volume fraction of mafic melt. For a 10% melt content, V_P and V_S may vary by 10–40% and 20–100%, respectively, depending on model assumptions. Given the known presence of magma beneath Kilauea, the anomalous *P* and V_P/V_S volumes can be reasonably ascribed to presence of partial melt.

Vertical cross sections of the *P*-wave velocity and V_p/V_s structures taken along a transect parallel to the southwest and upper east rifts further illustrate the primary features of the two structural models (Fig. 3). Also shown are the relocated hypocenters of events within a 4 km wide zone centered on the sections. Three clusters of events are observed, two of which are spatially correlated with the southern ring fracture system, and the third a more diffuse patch of events located at depths of 1 to 4 km beneath the upper east rift (Fig. 3*b*). These earthquakes reflect stress release associated with an increased magma production accompanying a strong, 4.5-hour-long inflation episode of the Kilauea summit in early February 1996 that produced a 22 μrad tilt change at Uwekahuna (see Fig. 13*a*).

It should be noted that the low *P*-wave anomaly beneath Puhimau crater (Fig. 3) imaged in the high-resolution model was not resolved in earlier regional models (ELLSWORTH and KOYANAGI, 1977; THURBER, 1984, 1987; ROWAN and CLAYTON, 1993; OKUBO *et al.*, 1997), because these former models did not have sufficient spatial sampling in the caldera region to identify anomalies with such small dimensions. However, the high-velocity anomalies within the upper 1 km, and at depth around the caldera in the high-resolution model are in agreement with regional models.

Spatio-temporal Properties of Long-period Seismicity Mapped with Small-Aperture Seismic Antennas

Small-aperture seismic arrays (seismic antennas) are useful for tracking the spatio-temporal properties of LP earthquakes and tremor. This type of seismicity cannot be located by conventional means because of the lack of impulsive phases in the records. The standard procedure is to compute frequency-slowness power spectra over successive short-time windows of array data. Assuming a finite number of plane waves are incident on the antenna, frequency-slowness spectra yield estimates of the directional properties of these plane waves, from which the locations of the strongest sources of seismic energy may be inferred using an appropriate structure model. Time-dependent changes in signal properties seen by the antenna are thus converted into time-dependent changes in source locations. Each plane wave moving across the antenna is defined by its ray parameter, *P*, where
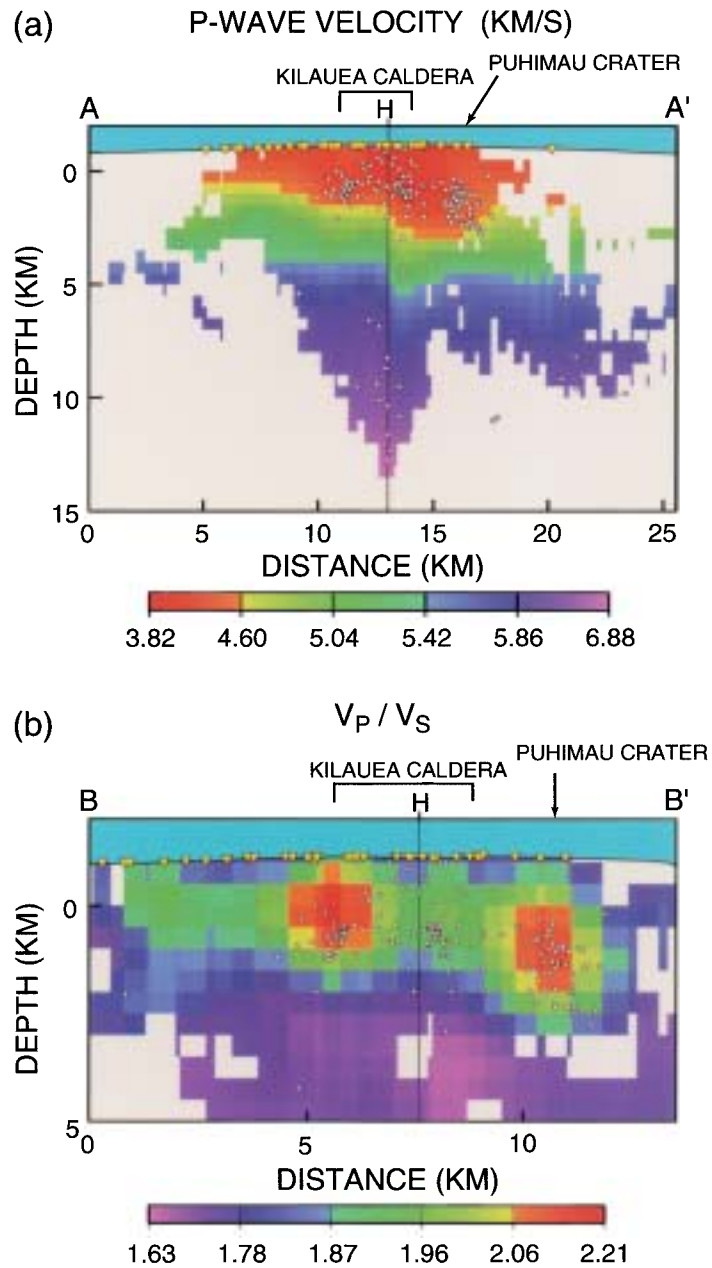
$$P = \sqrt{S_x^2 + S_y^2}$$

(a)

P-WAVE VELOCITY (KM/S)

(b)

V_P / V_S

Figure 3

Northeast-southeast cross sections for (a) *P*-wave velocity and (b) V_P/V_S models. The profile locations are shown in Figure 1; *H* and vertical line beneath indicate sharp bend in section (see Fig. 1). White circles indicate earthquake hypocenters located within ± 2 km of the profiles. Yellow inverted triangles mark the projections of stations onto the profiles. (From DAWSON *et al.*, 1999, after correction for an erroneous color scale in the original V_P/V_S panel.)

and azimuth, Φ, where

$$\Phi = \pi/2 - \arctan(S_y/S_x),$$

and S_x and S_y are the x and y components of slowness, respectively. The Cartesian coordinates are usually selected with the y axis pointing north and x axis pointing east. With this convention, Φ represents the apparent direction of propagation or signal azimuth measured clockwise from north.

Three small-aperture arrays of short-period seismometers were deployed near the Halemaumau pit crater and along the southern boundary of Kilauea caldera as part of a Japan-U. S. cooperative experiment conducted in February 1997 (Fig. 4). Array D has an aperture of 400 m and consists of 41 three-component sensors deployed in a semi-circular spoked pattern with station spacing of 50 m along the spokes and
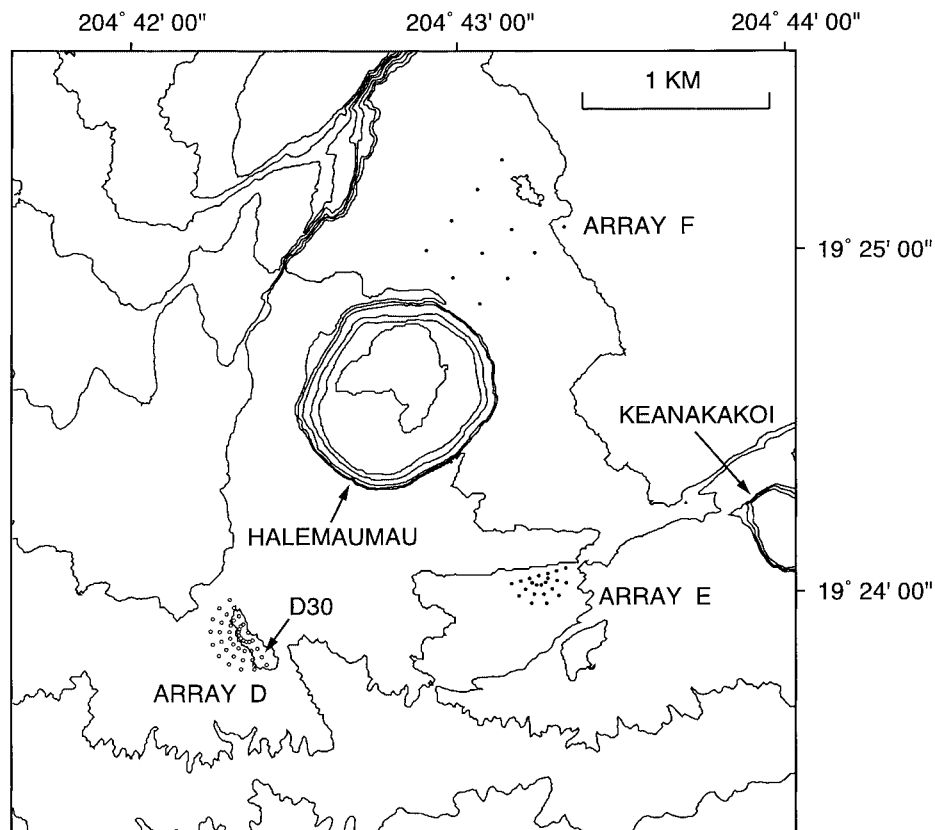
Figure 4
Map of the southern extent of the Kilauea caldera region showing locations of pit craters, main topographic features, and seismic antennas deployed during the 1997 Japan–U. S. experiment. Solid dots mark locations of vertical-component sensors and open circles indicate three-component sensors. Station D30 was used to obtain the seismograms displayed in Figure 5.

angular spacing of 20° between spokes. Array E, with an aperture of 300 m, includes 22 vertical-component sensors deployed in a similar pattern as array D with station spacing of 50 m along spokes but with a wider angular spacing of 30° between spokes. Array F is a polygonal array with approximate dimensions of 400 by 600 m and consists of three rows of 4 vertical-component receivers spaced roughly 200 m apart. The semi-circular geometry of arrays D and E was selected to enable both detailed frequency-slowness analyses of the wavefield and a quantification of the wavefield properties using the correlation method of AKI (1957, 1959, 1965), which is not discussed in this article. Details of the method can be found in AKI (1957) and in studies by FERRAZZINI et al. (1991) and CHOUET et al. (1998).

All the temporary stations deployed during the experiment used 16-bit, four-channel, Hakusan dataloggers. Three-component stations were equipped with Mark Products L22-3D sensors, and vertical-component stations were equipped with Mark Products L11-4A sensors. The seismometers had a natural frequency of 2 Hz and sensitivity of 0.5 V/cm/s, and were sampled at 100 samples/s/channel. All the array instruments used a common Global Positioning System (GPS) time base with an accuracy of 5 μs among all the channels.

The three arrays were deployed for the specific purpose of tracking LP events and tremor originating beneath Kilauea caldera. Figure 5 shows an 11-hour-long sample of vertical-component data recorded at one of the receivers in array D. This sample is representative of the seismicity of Kilauea at the time. Frequency-slowness analyses of the vertical-component data from the three arrays were performed using the Multiple Signal Classification (MUSIC) method (SCHMIDT, 1981, 1986; GOLD-STEIN and ARCHULETA, 1987, 1991a, b; GOLDSTEIN, 1988; GOLDSTEIN and CHOUET, 1994; CHOUET et al., 1997). The advantages of this method over more conventional array-processing techniques have been extensively discussed by GOLDSTEIN (1988) and GOLDSTEIN and ARCHULETA (1991a, b). Power spectra were computed for successive 2.56-s windows with 2.36 s of overlap spanning the array records. For data from arrays D and E, the power spectra were calculated over a bandwidth from 1 to 10 Hz using slowness stacking (SPUDICH and OPPENHEIMER, 1986). Both components of slowness were allowed to range over a 4 s km^{-1} window to insure the inclusion of both body and surface waves. Data from array F were processed in a similar manner over a reduced bandwidth of 1–6 Hz and narrower slowness range of 2 s km^{-1} because of this array's lack of resolution for frequencies above 6 Hz. Use of this array was restricted to the detection of body waves with ray parameters smaller than 1 s km^{-1}. The precision of ray parameter measurements, estimated according to eq. (12) in GOLDSTEIN and ARCHULETA (1991a), is approximately 0.05 s km^{-1} on array D, 0.09 s km^{-1} on array E, and 0.04 s km^{-1} on array F.

Figure 6 shows the temporal distributions of power, azimuth, and ray parameter for the vertical component of motion derived from the stacked slowness power spectra for a LP event recorded on array D. Errors were estimated by measuring the spread in azimuths and slownesses at a level of 90% of the peak spectral amplitude.
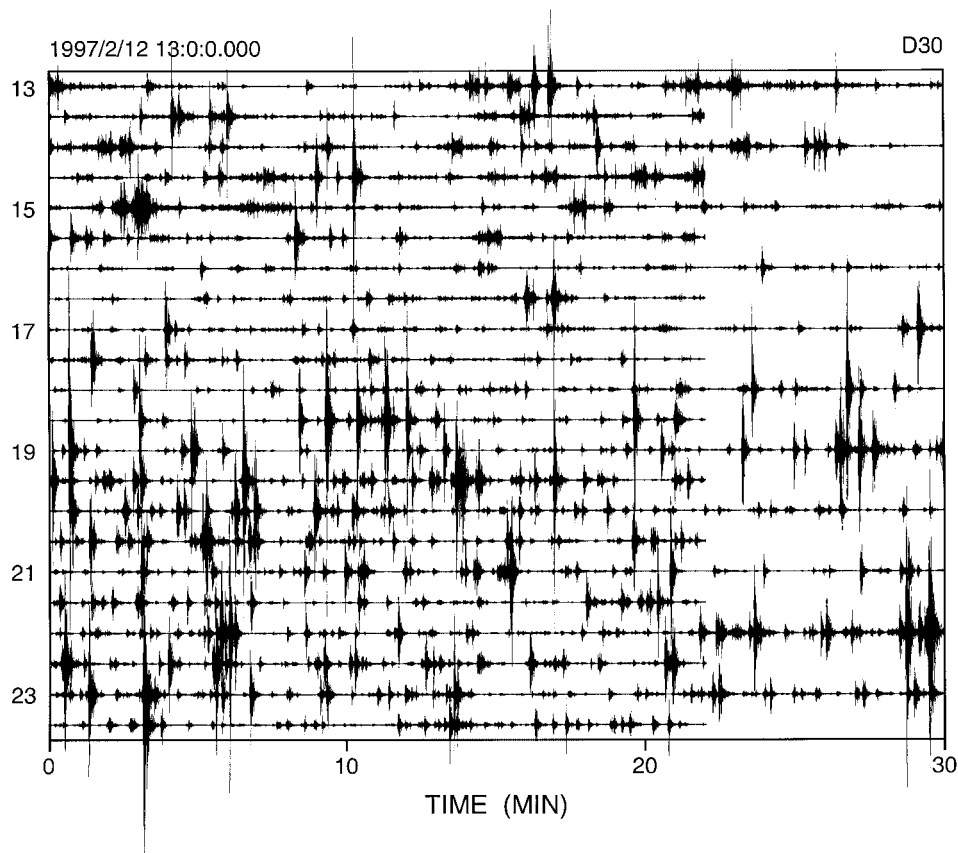
Figure 5

Typical vertical-component record (velocity) of LP seismicity selected for frequency-slowness analyses. The record is from station D30 of array D (see Fig. 4). Date and time (UT) at the start of the record are listed at the upper left of the plot. Numbers in the left margin indicate the start of individual hours in this recording period (beginning 1300, 12 February, 1997). Gaps in the record represent periods used by the data logger to perform GPS clock synchronization.

This method of error estimation is appropriate when there is a well-defined dominant spectral peak as seen near the onset of the LP event depicted. However, the error estimates obtained in such manner are less useful when dealing with the coda of the LP event, where multiple scattered arrivals with distinct azimuths and ray parameters are observed with roughly equal power above the 90% power level. This latter situation can lead to significant overestimation of the error as observed in the tail section of the record (Fig. 6). The 4.6-s time interval characterized by enhanced spectral power and stable azimuths was used to determine the directions of primary wave arrivals for this event.

Figure 7 shows the ranges of backazimuths for waves detected during 2–5 s bracketing the onset of the LP event. The backazimuths are obtained from
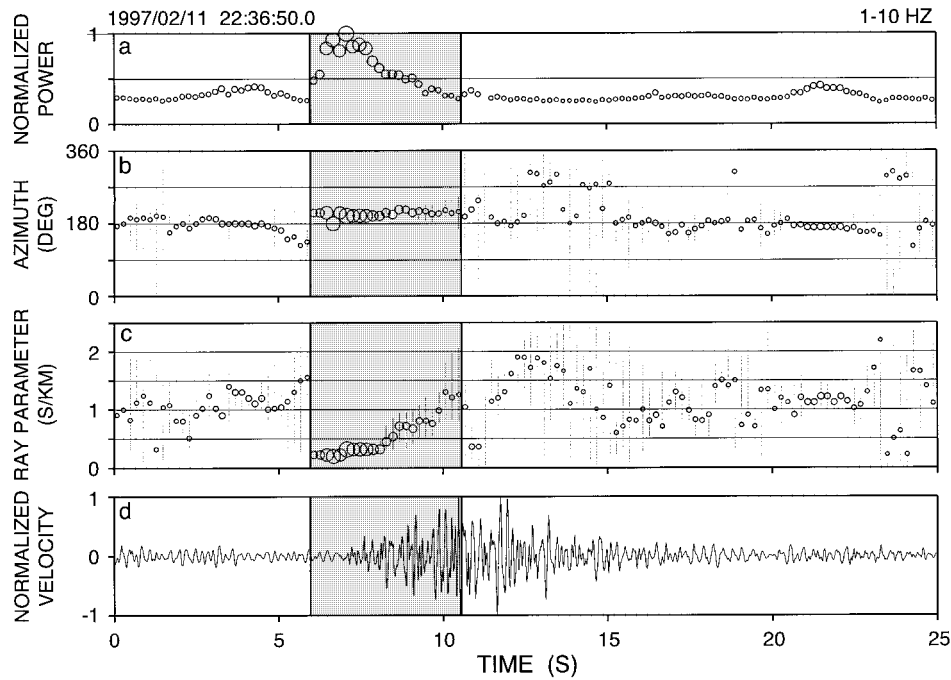
Figure 6

Peak spectral power, azimuth and ray parameter versus time obtained from frequency-slowness power spectra calculated for successive 2.56-s windows with 2.36 s of overlap ranging over 25 s of data for a LP event recorded on February 11, 1997. The plots show the results obtained for the vertical components of ground velocity recorded on array D. The bandwidth is indicated at the upper right, and the date and time at the start of the record are listed at the upper left. The vertical band of shading marks the time interval selected for measurements of azimuths and ray parameters associated with direct arrivals from the event shown in the bottom panel. (a) Power level of the dominant peak in individual stacked slowness spectra normalized by its maximum value reached during the entire interval depicted. (b) Azimuth, and (c) ray parameter versus time derived from the dominant peak in the stacked slowness power spectra calculated for individual windows. The sizes of the open circles in (a), (b), and (c) are proportional to the peak spectral power. (d) Vertical-component velocity seismogram from one of the receivers in array D.

frequency-slowness analyses performed simultaneously on data recorded with the three antennas. The intersection of the three colored wedges marks the most probable source region. First arrivals for 1129 LP events and 147 samples of tremor were detected by this method over a 23-hour period of swarm activity. With the exception of a few more distant events, this activity appears to originate from a region beneath and northeast of Halemaumau.

The geometrical method illustrated in Figure 7 provides only a rough idea of the epicentral source region because it does not take into account the distortion of the wavefield due to the volcanic structure. To improve the resolution of the source hypocenter, ray parameter and azimuth information from the three antennas must be interpreted in the context of a realistic model of the medium.
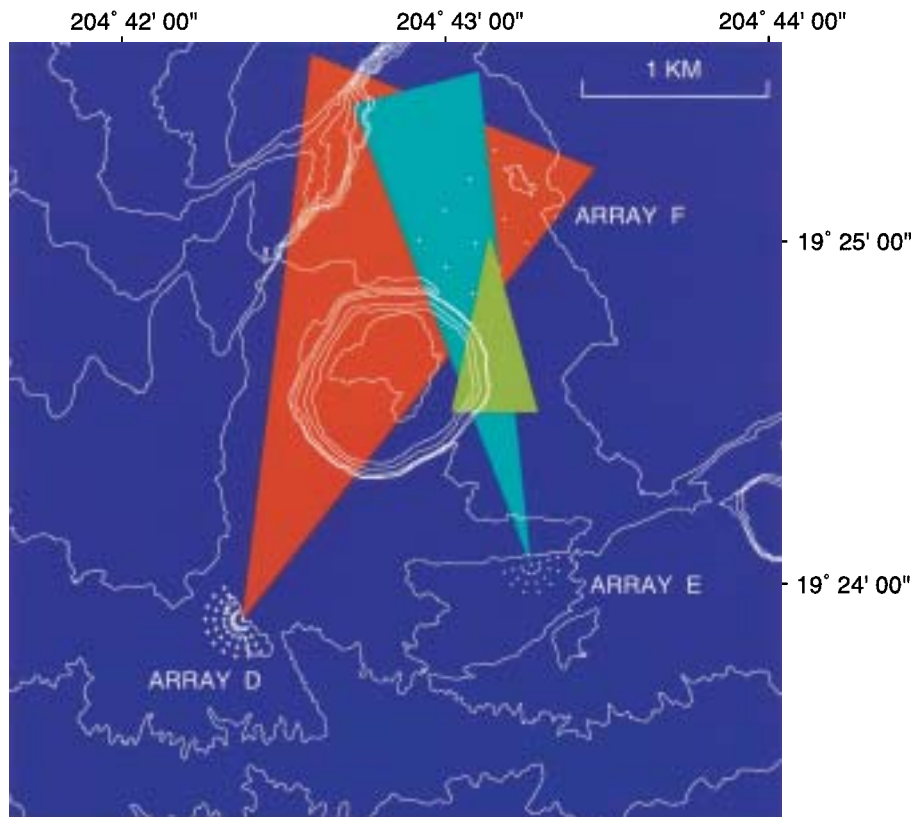
Figure 7
Map of the southern part of Kilauea caldera showing main topographic features, small-aperture arrays (D, E and F), and spread of backazimuths for direct waves propagating from a LP source (see event in Fig. 6d) detected by the three arrays. The domain defined by the intersections of the three wedges near the northeast boundary of Halemaumau encloses the most probable source epicenter.

A better estimate of the spatial extent of the source region of LP seismicity may be obtained by modeling the wavefield in the 3-D velocity structure and 3-D topography of Kilauea. Figure 8 illustrates the effect of topography on waves propagating from an isotropic point source located at a depth of 520 m below the northeast edge of Halemaumau. The medium is homogeneous with compressional and shear-wave velocities of 4 km/s and 2 km/s, respectively. The amplitude of the source dipole moment is 10^{12} N m and the source time function is a cosine-shaped pulse with period of 0.5 s. The snapshots (Fig. 8) represent the vertical component of ground displacement calculated by the finite-difference method of OHMINATO and CHOUET (1997). Diffraction of the incident P wave by the Halemaumau pit crater is observed as a distinct red patch at the base of Halemaumau and orange arcs extending from Halemaumau at $t = 0.5$ s. Wave diffraction by Halemaumau is also apparent in the snapshot at $t = 0.9$ s where it manifests as a notch of lighter blue in
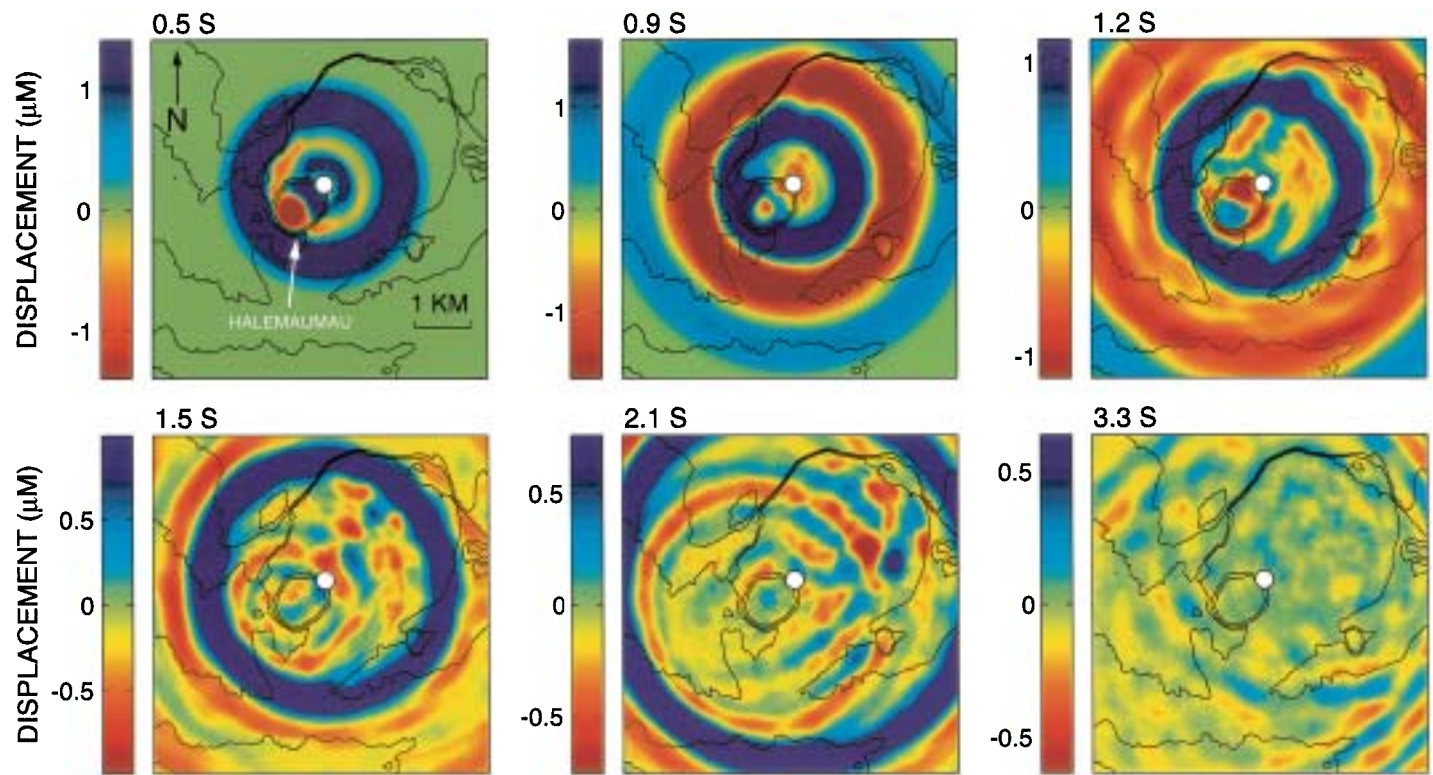
Figure 8

Snapshots showing wave propagation in the topography model of the Kilauea caldera region. Displayed is the vertical component of displacement at the surface of the medium. An isotropic point source is embedded at a depth of 520 m below the northeast edge of Halemaumau (see text for details). The white circle marks the source epicenter. The snapshots are superimposed on a map of Kilauea caldera (black contour lines with 50-m interval) to emphasize the effect of topography on waves propagating from the source. Colors indicate displacement amplitudes (in μ meters) according to the scale at the left of each snapshot. The medium is homogeneous and the observed wavefield complexity only reflects the effect of topography.

the dark blue ring marking the second peak of the wavefront near the southwest edge of the pit crater. The bright triangular orange patch observed near the source epicenter in this snapshot identifies converted SV waves reflected from the wall of Halemaumau facing the source. Waves are generated at the circular bottom corner of Halemaumau by the incident P wave. These waves travel along the floor of the pit crater where they interfere constructively to create a pattern of standing circular waves. These trapped waves are observed as a bright patch of orange near the center of Halemaumau at $t = 0.9$ s and appear as a bright orange ring coincident with the walls of Halemaumau at $t = 1.2$ s. Rayleigh waves scattered by the pit crater are observed as orange-colored rings propagating outward from Halemaumau at $t = 1.5$ s and $t = 2.1$ s. Wave diffractions by a smaller pit crater east of Halemaumau and by cliffs flanking the caldera to the north are observed in the snapshot at $t = 0.9$ s, where they appear as orange-colored notches embedded in the dark red ring identifying the trough in the P wavefront. Waves backscattered from cliffs marking the northwest caldera boundary appear as a linear band of orange oriented parallel to the topographic contours north of Halemaumau at $t = 1.2$ s. These waves propagate in a clockwise direction through the northern sector of the caldera where they interfere with the Rayleigh waves scattered by Halemaumau to produce a wave pattern identified by the orange patches located near the northern caldera boundary at $t = 1.5$ s and $t = 2.1$ s. Waves backscattered by cliffs flanking the northern sector of the caldera are also observed propagating southward past the southern edge of Halemaumau at $t = 3.3$ s. The mottled pattern of yellow on the caldera floor observed in this snapshot represents decaying standing waves resulting from the interference of waves backscattered by the topography of the caldera.

Figure 9 shows a snapshot of the free surface vertical displacement wavefield calculated for a medium including both topography and velocity structure. The compressional and shear-wave velocity structures are those derived by DAWSON et al. (1999) (see Figs. 2 and 3). The source is located at a depth of 200 m beneath the northeast edge of Halemaumau. The effect of velocity structure is a distortion of the features observed in the presence of topography alone. The arrows in Figure 9 represent the slowness vectors determined at three synthetic antennas whose locations and configurations simulate the setups of the three arrays deployed at Kilauea in February 1997 (see Fig. 4). The apparent slownesses and propagation azimuths of the waves are different in the model including topography only, compared to the model including both topography and structure. The differences between the slowness vectors derived from the two models are quite large and indicate that the combined effects of topography and structure must be taken into account to obtain an accurate location for the source.

The results from forward modelling of the wavefield depicted in Figure 9 can be used to invert the slowness data obtained from the three arrays. The procedure consists in a discretization of the source region using a uniformly spaced set of grid points in three dimensions, and computation of the free-surface responses produced by
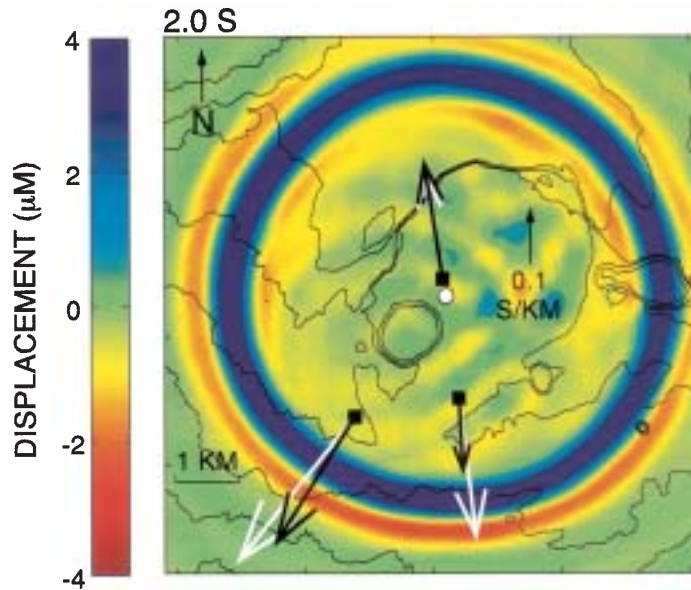
Figure 9

Snapshot of the vertical component of the free surface displacement wavefield 2.0 s after the origin time of a synthetic event. The medium includes both the topography and 3D velocity structure of Kilauea. An isotropic point source is embedded at a depth of 200 m below the northeast edge of Halemaumau. The source parameters are the same as those used in Figure 8 (see text for details). A white circle marks the source epicenter and black squares mark the locations of arrays D, E, and F (see Fig. 4). The arrows represent the slowness vectors estimated at the three arrays for a homogeneous medium including topography only (white arrows) and a medium including both topography and structure (black arrows). Differences are relatively large and affect both the azimuth and ray parameter. These results emphasize the importance of considering both topography and structure in the definition of a synthetic slowness vector model. Colors indicate displacement amplitudes (in μ meters) according to the scale at the left of the snapshot.

isotropic sources located at each grid node. Synthetic seismograms are calculated at three synthetic antennas that simulate the three arrays shown in Figure 4, and frequency-slowness analyses of the synthetic data yield estimates of ray parameters and azimuths at the three arrays for each point source. In this way, a three-dimensional slowness vector model is generated at each array from the grid of source positions.

The source locations of LP events and tremor are obtained in a probabilistic sense. First, a probability is assigned to every point in the source domain by comparing the results from the frequency-slowness analyses to the slowness vector model obtained for the domain. The statistical distributions of slownesses observed at each array for each individual LP event or tremor sample determine the shape of the probability functions. To each value in the slowness vector model corresponds, for each of the arrays, a given probability that can be mapped. The source location is obtained as the point corresponding to the maximum probability of the combined distributions for azimuths and ray parameters from the three arrays. As a final step,

the source location probability distributions for individual events are stacked to obtain an overall spatial probability distribution for the ensemble of events analyzed (see ALMENDROS et al., 2001a, b, for details). The distributions of probabilities for the locations of the sources of LP events and tremor are shown in Figure 10. The source regions of the two types of signals are defined as the volumes contained within the surfaces corresponding to 5% of the maximum of the stacked source location probability. The choice of 5% is conservative enough to include all the located hypocenters and provides maximum constraints on the sizes of the source regions.

The data illustrated in Figure 10 represent 83% of the total activity recorded during the 23 hours considered, hence these results provide a good representation of the overall behavior of the LP swarm. Figure 10a shows the source region of LP events. At least three different clusters of events are observed within this source volume. The most active cluster includes 857 hypocenters and is centered about 200 m northeast of Halemaumau at depths shallower than 200 m beneath the caldera floor (region A in Figs. 10b, c). A second cluster of 132 events is located at depths near 400 m beneath the northeast quadrant of Halemaumau (region B in Fig. 10c), and a third less dense cluster of 131 events is located at depths shallower than 200 m in an elongated zone extending southeastward from the northeast quadrant of Halemaumau. This latter region is seen in Figure 10a as the arm extending southeastward from Halemaumau; the northwest end of this arm is visible in the cutaway view in Figure 10c (region C). The individual clusters are not completely separated, and a few events do occur between these clusters, suggesting a connection between the different zones of high activity and providing a rough glimpse of the three-dimensional structure of the overall source region. Of the entire LP data set considered, only 9 events were found to be located outside of the source domain considered for analysis and these are not considered to be part of the LP source region. For the tremor the method reveals a single source region (Figs. 10d, e), which coincides with the most active source region of LP events northeast of Halemaumau

▶

Figure 10

Location and extent of the source region of long-period seismicity recorded at Kilauea Volcano in February 1997. (a) 3-D view of the source region of LP events. The source region is estimated as the region inside the surface corresponding to 5% of the maximum of the stacked source location probability obtained for 1120 LP events considered in the analysis. The horizontal projection of the source region and rim of the Halemaumau pit crater shown on the bottom of the cube provide additional information about the horizontal extent of this seismicity. (b) Cutaway view of the source region showing the most active source zone (A) located northeast of Halemaumau. (c) Secondary clusters of hypocenters (B, C) are also present at two depths beneath the crater. The maximum of the color scale is 0.3 in this panel. Accordingly, the probability is saturated in the main source region shown in (b). (d) 3-D view of the source region of tremor obtained from the surface of 5% of the maximum stacked probability corresponding to the 147 tremor samples considered. (e) Cutaway view of the stacked source location probability of tremor showing that there are no subregions and that the maximum probability occurs in a region (A') which coincides with the most active zone of LP event generation. (f) General view of the summit region. The blue cube shows the boundaries of the region extracted in (a)–(e). (Reproduced from ALMENDROS et al., 2001b.)
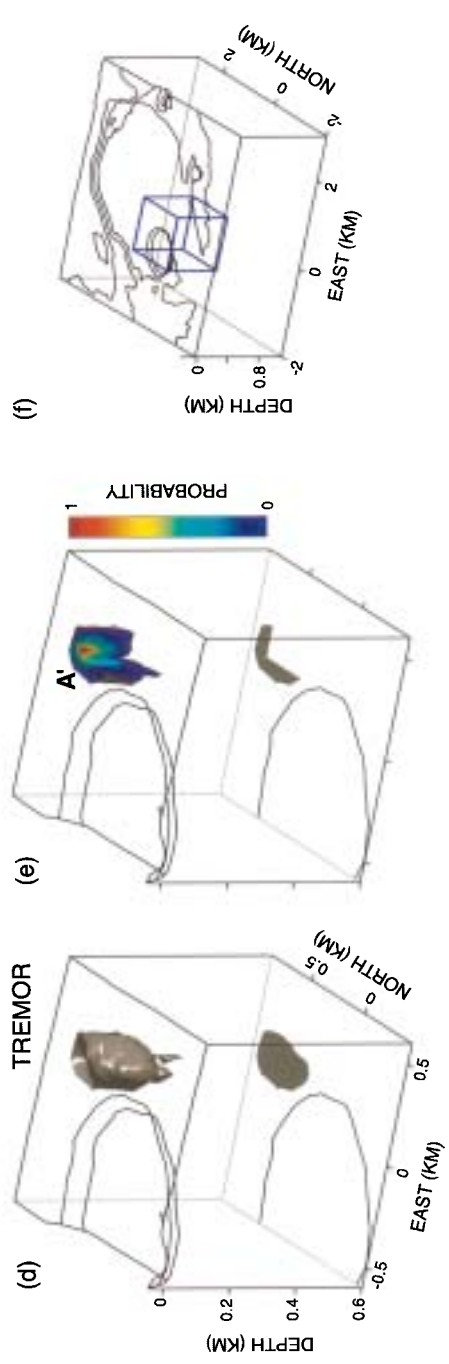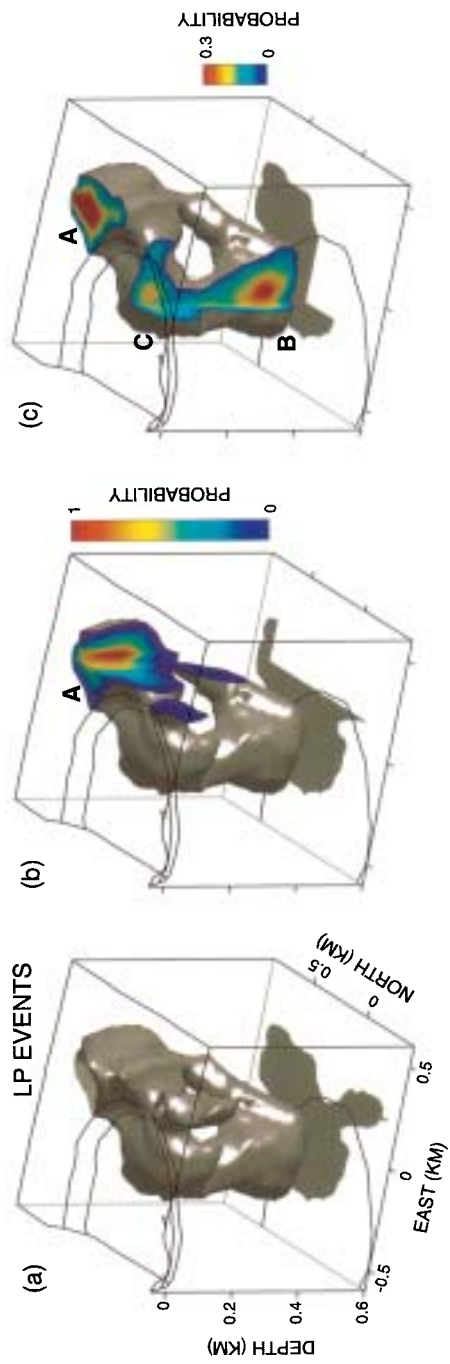
(compare A and A′ in Fig. 10). This result demonstrates the strong relation that exists between the two types of activities. The dimensions of the source regions in the east-west, north-south, and depth directions are roughly $0.6 \times 1.0 \times 0.5$ km for LP events and $0.2 \times 0.5 \times 0.2$ km for tremor, with volumes of 0.09 and 0.01 km^3, respectively. The locations, depths, and sizes of the source regions imaged in Figure 10 point to a hydrothermal origin for all the analyzed LP seismicity and suggest that this seismicity may reflect the response of Kilauea's hydrothermal system to enhanced degassing associated with increased magma transport in the deeper magma conduit. This deeper conduit system is discussed in more detail below.

Magma Pathway Geometry and Magma Volumetric Budget Derived from Moment Tensor Inversion of VLP Data

Broadband seismic observations carried out at many volcanoes (KAWAKATSU *et al.*, 1992, 1994, 2000; NEUBERG *et al.*, 1994; KANESHIMA *et al.*, 1996; OHMINATO and EREDITATO, 1997; OHMINATO *et al.*, 1998; DAWSON *et al.*, 1998; ROWE *et al.*, 1998; CHOUET *et al.*, 1999; ARCINIEGA *et al.*, 1999; FUJITA *et al.*, 2000; LEGRAND *et al.*, 2000; NISHIMURA *et al.*, 2000) clearly demonstrate the broadband nature of volcanic activity and undescore the usefulness of such measurements in the quantification of source mechanisms and mass transport phenomena associated with eruptive activity.

A broadband record obtained at Kilauea on February 1, 1996, shown together with filtered traces derived from this record (Fig. 11) is dominated by the oceanic microseismic noise with typical periods of 3–7 s. Most interesting is the displacement record obtained by filtering the signal with a 0.125-Hz low-pass filter, which displays a repetitive sawtooth signal with rise time of 2–3 min and drop time of 5–10 s. The repetitiveness of the VLP signal is a clear indication of the repeated action of a non-destructive source. Notice also the characteristic long-period signatures obtained by filtering the signal with a 0.33-Hz high-pass filter. These LP events display a fixed dominant frequency of 0.4 Hz, and their onsets coincide with the start of the downdrop segment in the VLP sawtooth displacement signals. This coincidence is strongly suggestive of a causative relationship between the VLP and LP signals.

The data in Figure 11 are part of a seismic sequence observed during a surge in the magma flow feeding the east rift eruption of the volcano (THORNBER *et al.*, 1996). The data were recorded by a 10-station broadband network deployed around Kilauea Caldera by the U.S. Geological Survey and by a Streckheisen STS-1 seismometer deployed at HVO by Caltech (Fig. 12). Typical bandwidths range from 0.04 s to 30, 100, 120, and 300 s.

The volcanic crisis at Kilauea on February 1, 1996 is characterized by a rapid summit inflation and increasing seismic activity starting at about 0800 Hawaiian Standard Time (HST). Figure 13a shows the tilt record obtained at the Uwekahuna
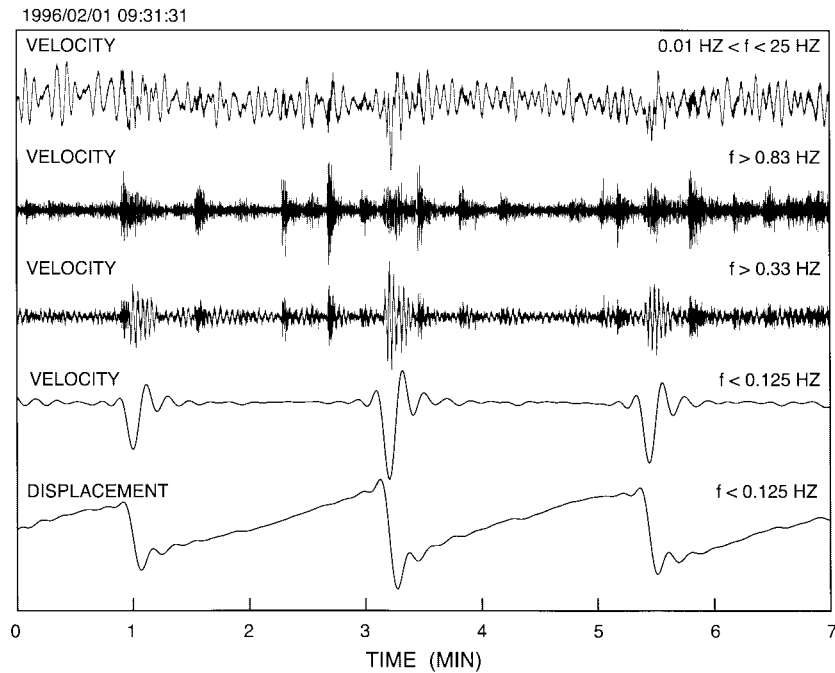
1996/02/01 09:31:31

Figure 11

Broadband record and associated filtered signals obtained at station GU9 of the Kilauea broadband network (Fig. 12) during a volcanic crisis on February 1, 1996. The broadband signal from the vertical component of velocity is filtered in various frequency bands to produce five records for the same 7-min time interval. The top trace shows the broadband signal ($0.01 < f < 25$ Hz), which is dominated by the oceanic wave-action microseism with periods in the range of 3 to 7 s. The second trace shows the signal after a high-pass filter has been applied ($f > 0.83$ Hz). The result is equivalent to a typical short-period record and shows a series of events superimposed on a background of tremor. The third trace also has a high-pass filter applied ($f > 0.33$ Hz); long-period (LP) signals with a dominant frequency of about 0.4 Hz are enhanced in this record. The fourth trace shows the signal when a low-pass filter is applied ($f < 0.125$ Hz); a repetitive very-long-period (VLP) signal consisting of pulses with period of about 20 s is observed. The fifth trace is the corresponding displacement record with a low-pass filter applied ($f < 0.125$ Hz), showing a repetitive sawtooth pattern with rise time of 2–3 min and drop time of 5–10 s. Notice that the onset of the LP signal observed above coincides with the onset of the downdrop in the VLP displacement. (Reproduced from DAWSON et al., 1998.)

vault near HVO. Summit inflation lasts approximately 4.5 hours, following which the summit deflates back to its original state over a 3-day period. Figure 13*b* shows details of the tilt signal and ground displacement at HVO observed during a 6-hour period starting at 0700 HST. The tilt reverses from inflation to deflation around 1230 HST. Figure 13*c* shows the details of the sawtooth displacement waveforms recorded at HVO and GU9 during a 15-minute period during inflation. Particle motions associated with the displacements observed on the broadband network are essentially linear and point to a source region beneath the northeast edge of Halemaumau (OHMINATO et al., 1998).
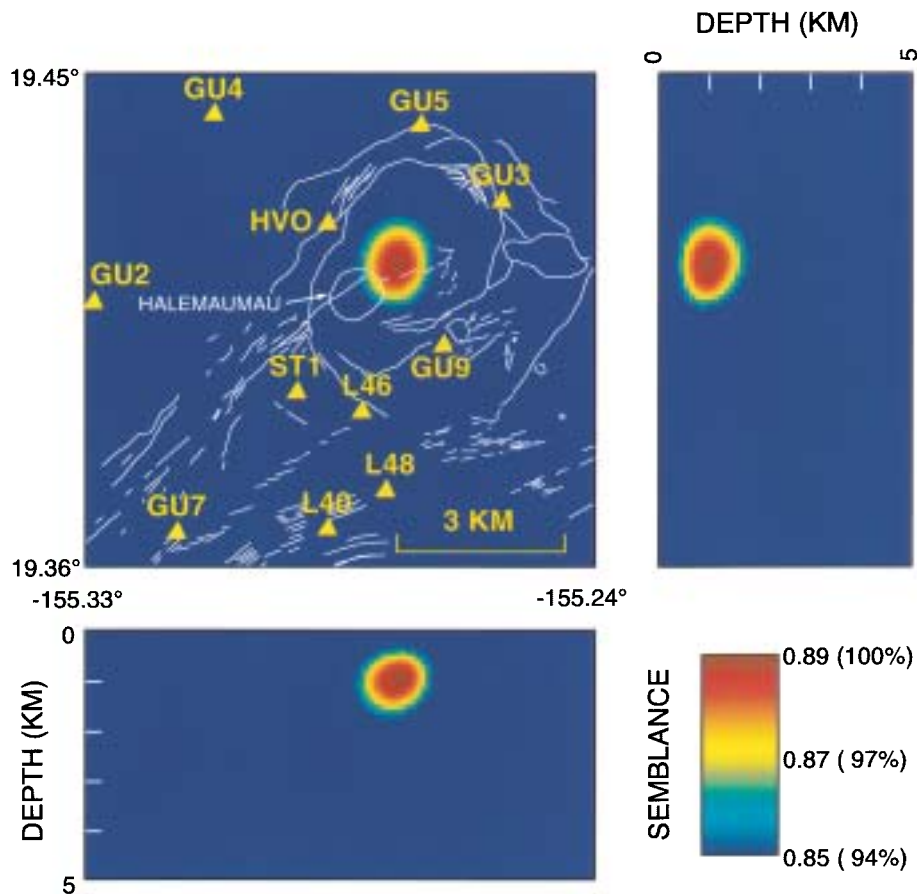
Figure 12

Map view and vertical cross sections of semblance distribution for the very-long-period signals observed at Kilauea on February 1, 1996 (see Fig. 11). Colors indicate semblance levels according to the scale at the bottom right. The map view shows the broadband seismic network at Kilauea. Solid triangles show station locations. Summit caldera, pit craters, faults, and fractures are shown by thin white lines. (Reproduced from OHMINATO *et al.*, 1998.)

A detailed analysis of these data was performed by OHMINATO *et al.* (1998). To locate the source OHMINATO *et al.* (1998) used the extended definition of semblance of MATSUBAYASHI (1995), which includes a penalty function that accounts for departures of the signal from perfect rectilinearity (see Appendix of OHMINATO *et al.*, 1998, for details). Figure 12 shows vertical and horizontal cross sections of semblance distribution for the VLP velocity pulses in Figure 11. The location of the peak of semblance points to a source hypocenter at a depth of roughly 1 km beneath the northeast edge of Halemaumau. OHMINATO *et al.* (1998) used this result
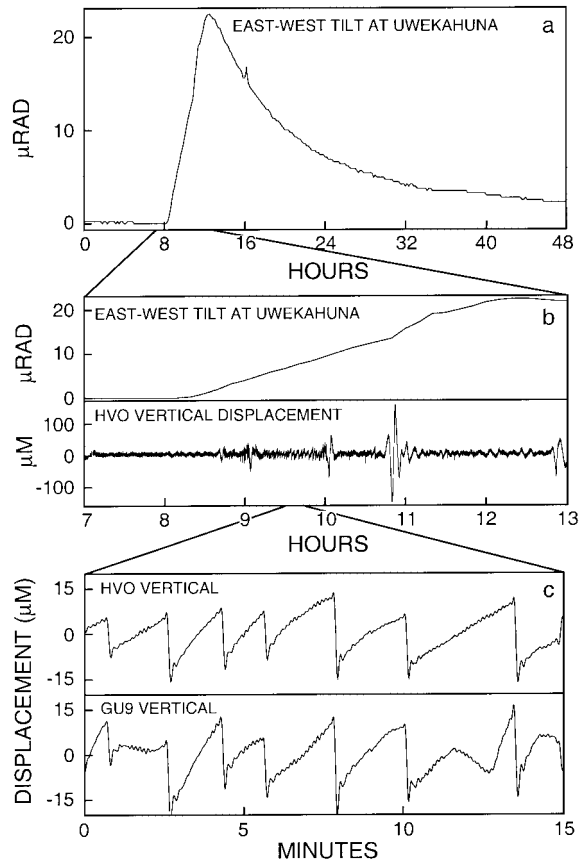
Figure 13

Tilt and displacements observed at Kilauea on February 1, 1996. (a) 48-hour-long record of tilt observed at the Uwekahuna vault near HVO. (b) Tilt at Uwekahuna and displacement at HVO observed over a 6-hour period starting at 0700 HST. (c) Sawtooth displacement waveforms recorded at HVO and GU9 (Fig. 12). Only the vertical component is shown as the radial displacement displays essentially the same waveform owing to the linearity of particle motion. (Reproduced from OHMINATO et al., 1998.)

as an initial source location in their inversion of the observed waveforms for source mechanism.

OHMINATO et al. (1998) carried out their inversion assuming a point source embedded in a homogeneous half space with compressional wave velocity $V_P = 3$ km/s, shear-wave velocity $V_S = V_P/\sqrt{3}$ km/s, and density $\rho = 2.7$ g/cm^3. They considered three cases including (1) a purely volumetric source, (2) a source including six moment tensor components but no single force, and (3) a source including six moment tensor components and three single force components. Inversions performed under the assumption of purely volumetric tensor components M_{xx}, M_{yy} and M_{zz} resulted in poor fits of the observed waveforms. The waveform

match was significantly improved when six moment tensor components, but no single force, were included in the source mechanism. However, residual errors were still found to be high, suggesting that some stations were not well explained. Only in the last case, in which six moment tensor components and three single force components were used to express the source mechanism, were the residual errors observed to be significantly reduced. OHMINATO et al. (1998) evaluated each model by calculating the Akaike Information Criterion (AIC) (AKAIKE, 1974). They found the minimum value of the AIC for case 3, confirming that the error reduction was not solely a result of the increase in the number of free parameters used in the model. Figure 14 shows that the waveforms are generally well reproduced by inversion of the VLP data assuming six moment tensor components and three single force components. Figure 15 shows the corresponding source mechanism. Note that the volumetric components of the moment tensor clearly dominate in these solutions. There is also evidence of the presence of a single force whose contribution to the observed waveforms is roughly 10% in amplitude.

The source model derived from these data is displayed in Figure 16. The solution shows a compression of the source in all directions, with a dominant eigenvector slightly inclined from the vertical direction. The amplitude ratios for the three axes of the moment tensor are roughly 1:1:2, hence the solution can be interpreted as representative of a sub-horizontal crack or sill-like structure if one assumes a Poisson ratio $v = 1/3$ in the source region. The volume change estimated from the moment is about 3000 m^3. As the amplitude of the signal varies from sawtooth to sawtooth, the volume estimated for individual sawtooths ranges from 1000 to 4000 m^3. The volume budget obtained by integration over the total duration of VLP seismic activity is on the order of 500,000 m^3.

As indicated above, the inversion results also provide evidence for the presence of a single force in the source mechanism of the VLP events at Kilauea. A single force can be generated by a linear exchange of momentum between the source volume and the rest of the earth (TAKEI and KUMAZAWA, 1994). For example, a vertical single force may be generated as a consequence of the release of gravitational energy in the source volume. Such situation occurs during the ascent of a slug of gas in a column of liquid. As the slug rises toward the surface, liquid moves downward to fill the void left behind by the ascending gas. The sinking of dense liquid associated with the ascent of less dense gas changes the density structure of the fluid column and releases gravitational energy. Another example of vertical single force is the recoil force generated by a volcanic jet during an eruption (KANAMORI et al., 1984; CHOUET et al., 1997). The shear traction due to the flow of viscous liquid in a conduit provides yet another means to generate a single force (CHOUET, 1996b). In the inversion results shown in Figure 15, the force is synchronous with the compression of the crack, consistent with a discharge of fluid from the crack. OHMINATO et al. (1998) attributed the origin of this force to the drag force generated by the flow of viscous magma through a narrow constriction in the flow path.
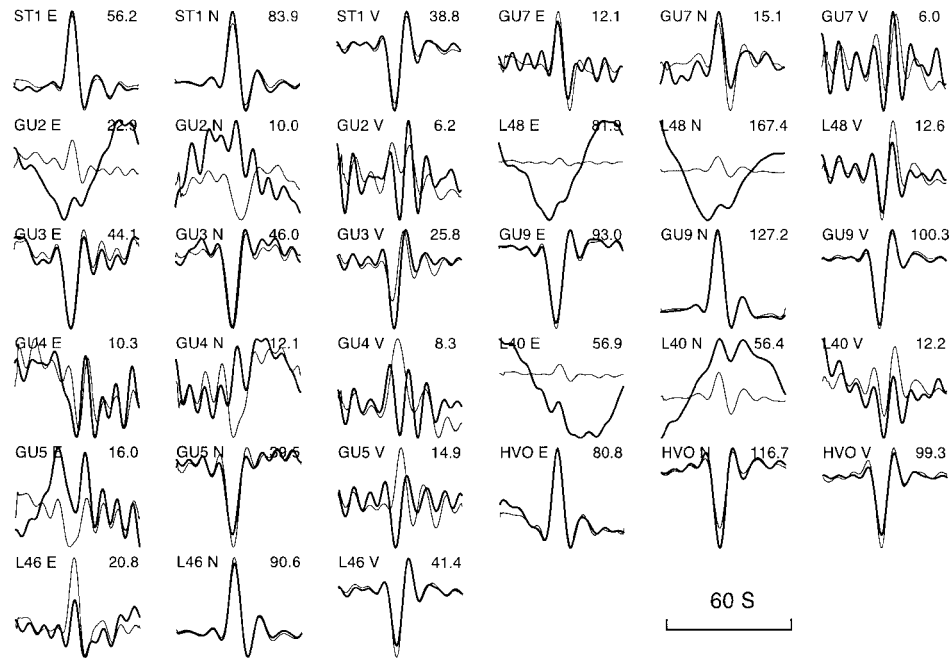
Figure 14

Waveform match obtained for a point source with mechanism consisting of six moment tensor components and three single forces. Horizontal components at GU2, L48, and L40 were not included in the inversion because these traces are contaminated by noise. The source is embedded at a depth of 1 km in a homogeneous half space. Thin and bold lines represent synthetics and data, respectively. The station code and component of motion are indicated at the upper left of each seismogram. Numbers at the upper right of the seismograms indicate the peak to peak amplitudes of the seismograms in units of 10^{-7} m/s. (Reproduced from OHMINATO *et al.*, 1998.)

Momentum conservation in the overall source-earth system requires that the drag force generated by viscous fluid flow in the conduit must be counterbalanced by a force in the opposite direction. Such restoring force is not apparent in the F_z component in Figure 15. One possible explanation for this may be that the compensating force is generated by a slow process operating over a time scale that is beyond the responses of the broadband seismometers monitoring Kilauea.

A conceptual model which may explain both seismic data and total lava flow is shown in Figure 17. The mechanism involves the injection of a large slug of gas from the summit magma reservoir into the crack. Both liquid magma and gas flow through a narrow constriction at the crack outlet. Initially, liquid magma occupies the entire outlet cross section and gas accumulates in the crack, deforming the crack walls as the back pressure of gas increases in the crack. Eventually, the gas slug deforms and rapidly squeezes past the constriction along with the liquid, triggering the rapid deflation of the crack in the process. This sequence is repeated with successive slugs. In this model, the restraining force of the liquid on the gas slug acts like a self-

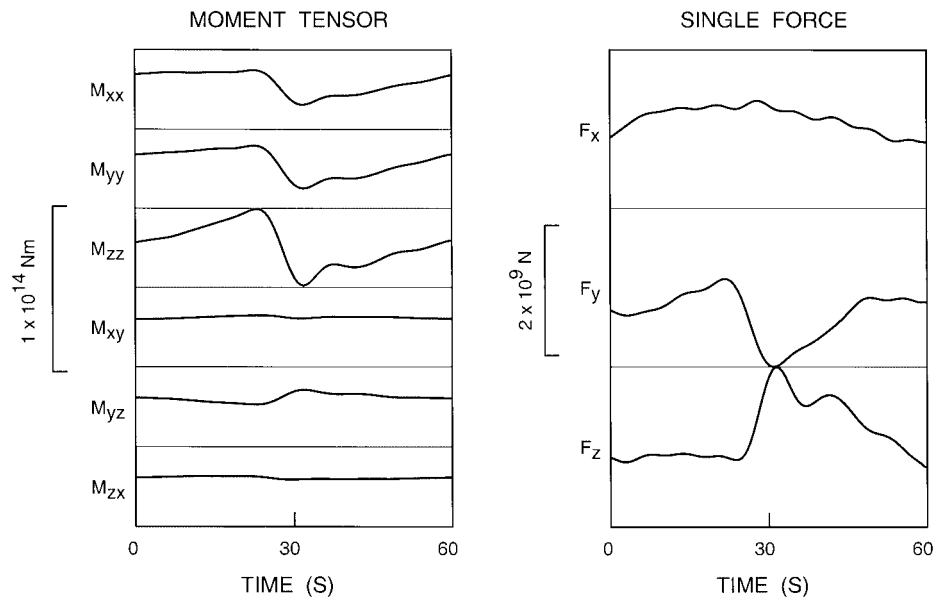MOMENT TENSOR   SINGLE FORCE

Figure 15
Source time functions obtained for a point source with mechanism consisting of six moment tensor components and three single forces. (Reproduced from OHMINATO et al., 1998.)
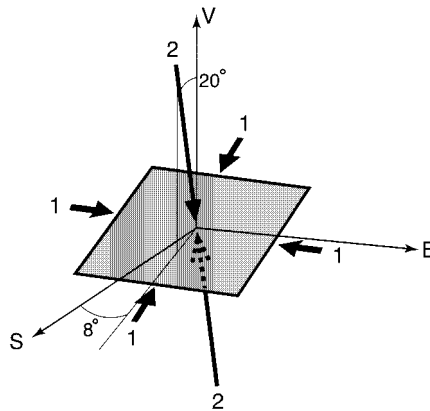
Figure 16
Source model obtained from inversion of VLP data at Kilauea. The amplitude ratios for the three axes of the moment tensor are 1:1:2. This solution is representative of a subhorizontal crack if one assumes a Poisson ratio $v = 1/3$ in the source region. (Reproduced from OHMINATO et al., 1998.)

activated viscosity-controlled valve. In the stratified flow through the nozzle, the liquid moves at a steady slow pace on the order of m/s but the gas flow itself is choked in the narrow opening between the liquid/gas interface and the upper wall
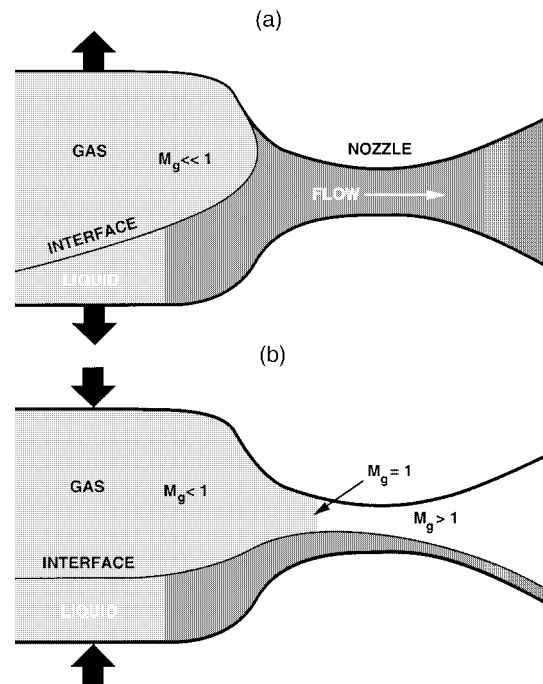
Figure 17

Conceptual model of separated gas-liquid flow through a converging-diverging nozzle under choked conditions (after WALLIS, 1969, pp. 71–74). (a) Inflation phase showing gas accumulating upstream of the nozzle and building excess pressure and deforming the crack as a result. The gas slug is essentially stationary and the Mach number of the gas is $M_g \ll 1$. This phase coincides with the upgoing ramp in the observed sawtooth displacement signals. (b) Separated gas-liquid flow through the nozzle under compound choked conditions. The gas flow is choked ($M_g = 1$) in the nozzle defined by the liquid-gas interface and upper solid wall, and is supersonic ($M_g > 1$) immediately downstream of the nozzle. There is a maximum possible gas flow rate which is fixed by the rate of liquid discharge for given upstream conditions and fixed throat geometry. In the limit, liquid fills the duct entirely, and there is no gas flow. (Reproduced from OHMINATO et al., 1998.)

(WALLIS, 1969). The formation of a shock associated with compound choking of the flow may act as a trigger of acoustic oscillations of the liquid/gas mixture which may be at the origin of the LP event with characteristic resonant frequency of 0.4 Hz observed in conjunction with the rapidly downgoing part of the sawtooth displacement signals shown in Figure 11.

Distinct VLP waveforms were again observed during a reinflation of the Kilauea summit following a 30 μrad deflation episode on January 29–30, 1997 (unpublished data, USGS Hawaiian Volcano Observatory). During February 1997, periods of inflation and minor deflation were observed, and each time a sharp transition from deflation to inflation occurred, VLP waveforms with periods of 30–40 s were detected by the Kilauea broadband network (Fig. 29a). As seen in the volcanic crisis of February 1, 1996, the VLP velocity waveforms observed in February 1997 share

common features among each other, pointing again to a process involving the repeated activation of a fixed source. Particle motions associated with each pulse are approximately linear, exhibiting compressional motion at all stations, and analyses of semblance and particle motion are consistent with a point source located 1 km beneath the northeast edge of Halemaumau. Moment tensor inversions of these data are well explained by a transport mechanism operating on a crack linking the summit reservoir to the east rift of Kilauea. The crack location is similar to that of the crack activated during the inflation episode on February 1, 1996 (see Fig. 12), although the transport mechanism involved in the two sources is different (CHOUET and DAWSON, 1997). The proximity of the two sources observed in 1996 and 1997 points to a reactivation of a permanent plexus of cracks in a restricted source zone below the northeast edge of Halemaumau. As seen in Figures 10 and 12, the magma conduit imaged from VLP data lies directly beneath the source of hydrothermal energy imaged from LP seismicity. The unsteady magma transport accompanying summit reinflation in February 1997, and concurrent shallow hydrothermal activity immediately above the magma conduit, therefore are strongly suggestive of a dynamic link between the magmatic and hydrothermal systems beneath Halemaumau. Accordingly, enhanced hydrothermal activity may be viewed as the result of an increased flow of heat into the base of the hydrothermal system resulting from an increase in the discharge of magmatic gases through the fractured rock mass capping the magma conduit.

Acoustic Properties of Magmatic and Hydrothermal Fluids Derived
from Spectral Analyses of LP Events

Long-period seismicity, including LP events and tremor, has been widely observed in relation to magmatic and hydrothermal activities in volcanic areas and has been recognized as a precursory phenomenon for eruptive activity (CHOUET et al., 1994; CHOUET, 1996a). The waveform of the LP event is characterized by simple decaying harmonic oscillations except for a brief time interval at the event onset (Fig. 18). This characteristic signature is commonly interpreted as oscillations of a fluid-filled resonator in response to a time-localized excitation. By the same token, tremor may be viewed as oscillations of the same resonator in response to a sustained excitation. LP events are particularly important in the quantification of volcanic and hydrothermal processes, because the properties of the resonator system at the source of this event may be inferred from the complex frequencies of the decaying harmonic oscillations in the tail of the seismogram. The damped oscillations in the LP coda may be characterized by two parameters, f and Q. The constant f is the frequency of the dominant mode of oscillation, and the parameter Q represents the quality factor of the oscillatory system. The observed Q of LP events may be expressed as
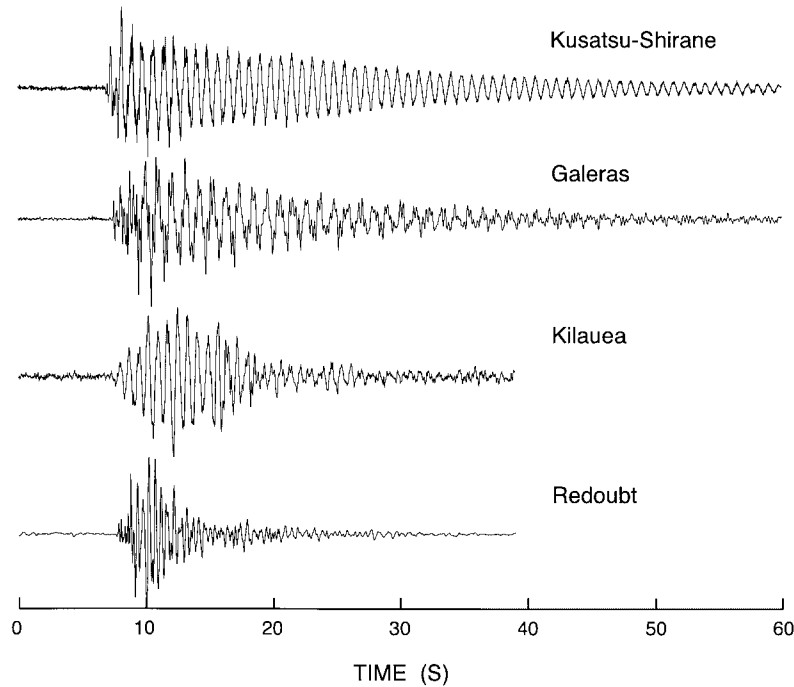
Figure 18

Typical signatures of long-period events observed at Kusatsu-Shirane, Galeras, Kilauea and Redoubt volcanoes. The signatures are all characterized by a harmonic coda following a signal onset enriched in higher frequencies. (Reproduced from KUMAGAI and CHOUET, 1999.)

$$Q^{-1} = Q_r^{-1} + Q_i^{-1}, \tag{3}$$

where Q_r^{-1} and Q_i^{-1} represent the radiation and intrinsic losses, respectively (AKI, 1984). Typical frequencies observed for LP events are in the range 0.5–5 Hz (CHOUET, 1996a), and typical observed Q range from values near 1 to values larger than 100. For example, the events at Kilauea and Redoubt in Figure 18 are representative of values of Q between 20 and 50, and the events at Kusatsu-Shirane and Galeras are characterized by values of Q higher than 100.

To compare the complex frequencies of LP events with those predicted by a resonator model we use a crack geometry, which is appropriate for mass transport conditions beneath a volcano. The fluid-filled crack model was originally proposed by AKI et al. (1977b) and has been extensively studied by CHOUET (1986, 1988, 1992) using a more detailed description of the coupling between fluid and solid. Chouet's studies showed that the fluid-filled crack generates a very slow wave propagating along the crack wall, which he called the "crack wave." The asymptotic behavior of this wave for a crack of infinite length was investigated by FERRAZZINI and AKI (1987) in an analytical study of normal modes trapped in a liquid layer sandwiched

between two solid half spaces. The crack wave leads to more realistic estimates of the size of the resonator as compared to a resonator with spherical geometry (CROSSON and BAME, 1985; FUJITA et al., 1995). Chouet's model consists of a rectangular crack with length L, width W, and aperture d, containing a fluid with acoustic velocity a and density ρ_f, embedded in an elastic solid with compressional velocity α and density ρ_s (Fig. 19). The crack is excited into resonance by a pressure transient applied symmetrically over small areas of the crack walls near the center of the crack. A solution of the coupled equations of fluid dynamics and elastodynamics is obtained by finite differences. Note that the crack model does not account for dissipation mechanisms within the fluid so that simulations done with this model predict quality factors due to the radiation loss only. Intrinsic losses are treated separately.

Once the space-time motion of the crack wall is obtained in response to the pressure transient, the ground response due to a fluid-driven crack embedded in a homogeneous or layered half space can be easily synthesized using the discrete wavenumber method (BOUCHON, 1979, 1981) and propagator-based formalism of CHOUET (1987). Figure 20a shows a vertical velocity waveform calculated at the free surface in the near field of a resonating fluid-filled crack embedded in a homogeneous half space. Figure 20b shows the results from a Sompi analysis of the synthetic waveform in the form of a frequency–growth rate $(f - g)$ diagram (KUMAZAWA et al., 1990). Densely populated regions in the $f - g$ diagram represent the signal for which the complex frequencies are stably determined for different autoregressive (AR) orders (KUMAZAWA et al., 1990), while scattered points represent incoherent noise. Figure 20c shows the corresponding normalized FFT spectrum. As can be
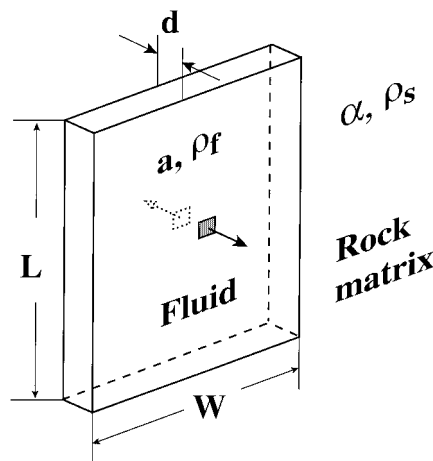

Figure 19
Geometry of the fluid-filled crack model. The crack has length L, width W, and aperture d, and contains a fluid with sound speed a and density ρ_f. The crack is embedded in a solid with compressional wave velocity α and density ρ_s. Excitation of the crack is provided by a pressure transient applied symmetrically on both walls over the small areas indicated by the grey patches near the center of the crack.
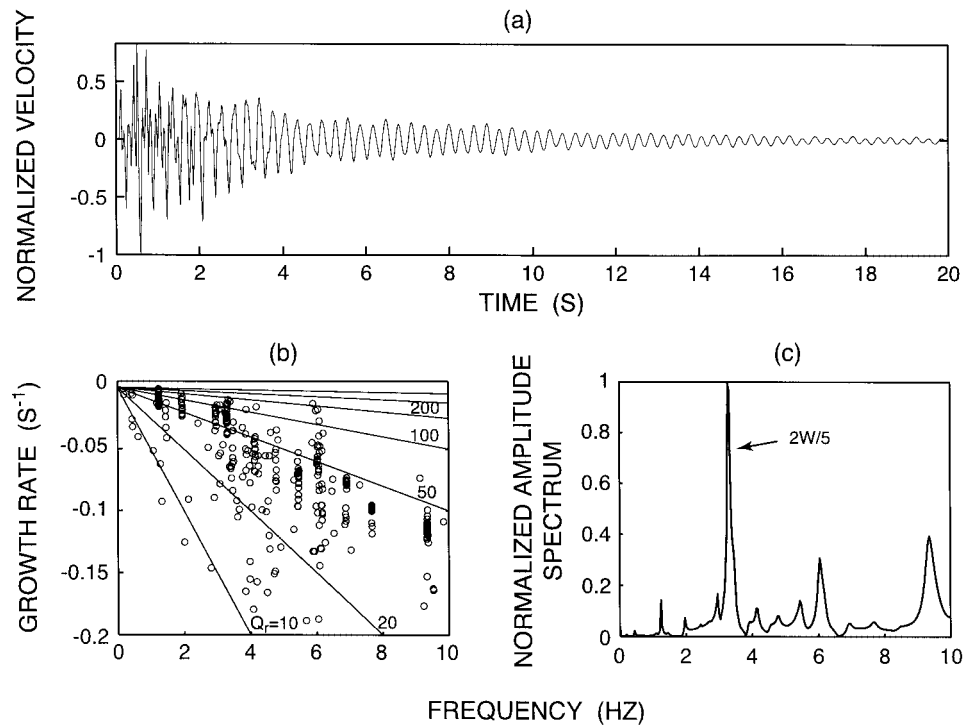
Figure 20

(a) Synthetic velocity waveform observed at an epicentral distance of 500 m and azimuth $\phi = 45°$ measured from the crack trace for a vertical crack (vertical extent $L = 150$ m and horizontal extent $W = 75$ m) buried at a depth of 500 m. The aspect ratio is $L/d = 10^4$, and the parameters of the fluid and solid are $a = 300$ m/s, $\rho_f = 2120$ kg/m^3, and $\alpha = 4500$ m/s, $\rho_s = 2650$ kg/m^3. (b) Plots of the complex frequencies of wave elements for all trial AR orders estimated for the waveform in (a). The straight lines represent lines along which the Q_r factor is constant. (c) Normalized amplitude spectrum corresponding to the waveform in (a). (Reproduced from KUMAGAI and CHOUET, 2000.)

readily seen in Figures 20*b* and 20*c*, there are four dominant peaks and other minor peaks in the 0–10 Hz frequency range, which show an almost constant Q_r factor due to radiation near 50. The peak at frequency near 3.5 Hz corresponds to the transverse mode with wavelength $2W/5$. This mode was used by KUMAGAI and CHOUET (2000) to examine the dependence of the complex frequency on the parameters α/a and ρ_f/ρ_s.

Using the Sompi method KUMAGAI and CHOUET (2000) estimated the factor Q_r and dimensionless frequency $v = fL/\alpha$ of the mode $2W/5$ for α/a ranging from 5 to 45 and ρ_f/ρ_s ranging from 0.05 to 1. The results of their study are shown in Figure 21. The factor Q_r monotonically increases with increasing α/a, and slightly increases with decreasing ρ_f/ρ_s. Thus, Q_r increases with increasing impedance contrast $Z = \alpha\rho_s/(a\rho_f)$, although Q_r more strongly depends on α/a than on Z. The dimensionless frequency v decreases with increasing α/a and ρ_f/ρ_s, and depends

equally on both of these parameters. The fluids considered are mixtures of gas, liquid, and solid, including gas-gas mixtures ($H_2O - CO_2$), liquid-gas mixtures (water $- H_2O$, basalt $- H_2O$), and dusty and misty gases (ash $- SO_2$, water droplet $- H_2O$). Sound speeds and densities of bubbly liquids (gas-volume fractions less than 10%) were estimated using the Van Wijngaarden-Papanicolaou model (COMMANDER and PROSPERETTI, 1989). For the acoustic properties of foams (gas-volume fractions between 10 and 90%), KUMAGAI and CHOUET (2000) used the adiabatic equation of state for liquid and gas derived by KIEFFER (1977). The acoustic properties of gas-gas mixtures were derived using the ideal mixing theory (e.g., MORRISSEY and CHOUET, 2001), and those of dusty and misty gases (ash $- SO_2$ gas and water droplet $- H_2O$ gas mixtures) were calculated using the model of TEMKIN and DOBBINS (1966). The range of acoustic properties used by KUMAGAI and CHOUET (2000) for the crack model covers almost the entire ranges of α/a and ρ_f/ρ_s for the various types of fluids, with the exception of dusty gases containing very small weight fractions of pure gas for which α/a may reach values up to nearly 60.

Figure 22 shows examples of synthetic far-field P wavetrains that would be generated in an infinite homogeneous medium. These waveforms represent the impulse response of a fluid-filled crack containing different types of fluids. The crack geometry and spatio-temporal properties of the applied excitation are identical in all the examples shown. Each signal shows distinct resonance characteristics, suggesting that LP signatures may be used to constrain the fluid composition at the source.

A comparison of Q_r^{-1} with Q_i^{-1} in bubbly fluids is shown in Figure 23. The estimates of Q_i^{-1} represent the contributions from three damping mechanisms, namely, viscosity, heat transfer, and acoustic radiation. In bubbly water as in bubbly basalt, Q_i^{-1} becomes comparable to or larger than Q_r^{-1} in fluids containing bubbles whose radii are larger than 1 mm. Intrinsic absorption becomes trivial in fluids containing bubbles with radii smaller than 0.3 mm so that Q becomes essentially equivalent to Q_r in such fluids.

Figure 24 shows a comparison of Q_r^{-1} with Q_i^{-1} in dusty and misty gases. The estimates of Q_i^{-1} represent the combined loss mechanisms of viscosity and thermal diffusion. The factor Q_i^{-1} in dusty gases containing particles with radii larger than 10 μm is comparable or larger than Q_r^{-1}. For solid particles with sizes 1 μm or less intrinsic absorption is trivial. Similar results are observed in a misty gas where intrinsic

▶

Figure 21

Plots of α/a versus ρ_f/ρ_s curves for various types of fluids, and Q_r and v contours for the crack model. Solid dots mark points where the synthetic waveforms are calculated. The contour plots of Q_r and v (yellow curves) are obtained by fitting quadratic polynomials to the calculated Q_r or v values along profiles with constant ρ_f/ρ_s. Dashed, solid, and dash-dotted lines indicate α/a and ρ_f/ρ_s calculated for fluids at pressures of 5, 10, and 20 or 25 MPa, respectively, using $\alpha = 2700$ m/s, $\rho_s = 2500$ kg/m^3 at 5 MPa pressure, $\alpha = 4000$ m/s, $\rho_s = 2650$ kg/m^3 at 10 MPa pressure, and $\alpha = 5000$ m/s, $\rho_s = 2700$ kg/m^3 at 20 and 25 MPa pressure. Thermodynamic properties of the fluids can be found in KUMAGAI and CHOUET (2000). (Reproduced from KUMAGAI and CHOUET, 2000.)

absorption becomes trivial in the presence of water droplets with sizes 10 μm or less, but may dominate when water droplets of 100 μm or larger are present. Thus, dusty gases containing small-size particles or misty gases containing small-size droplets can both generate long-lasting oscillations characterized by large values of Q_r ranging up
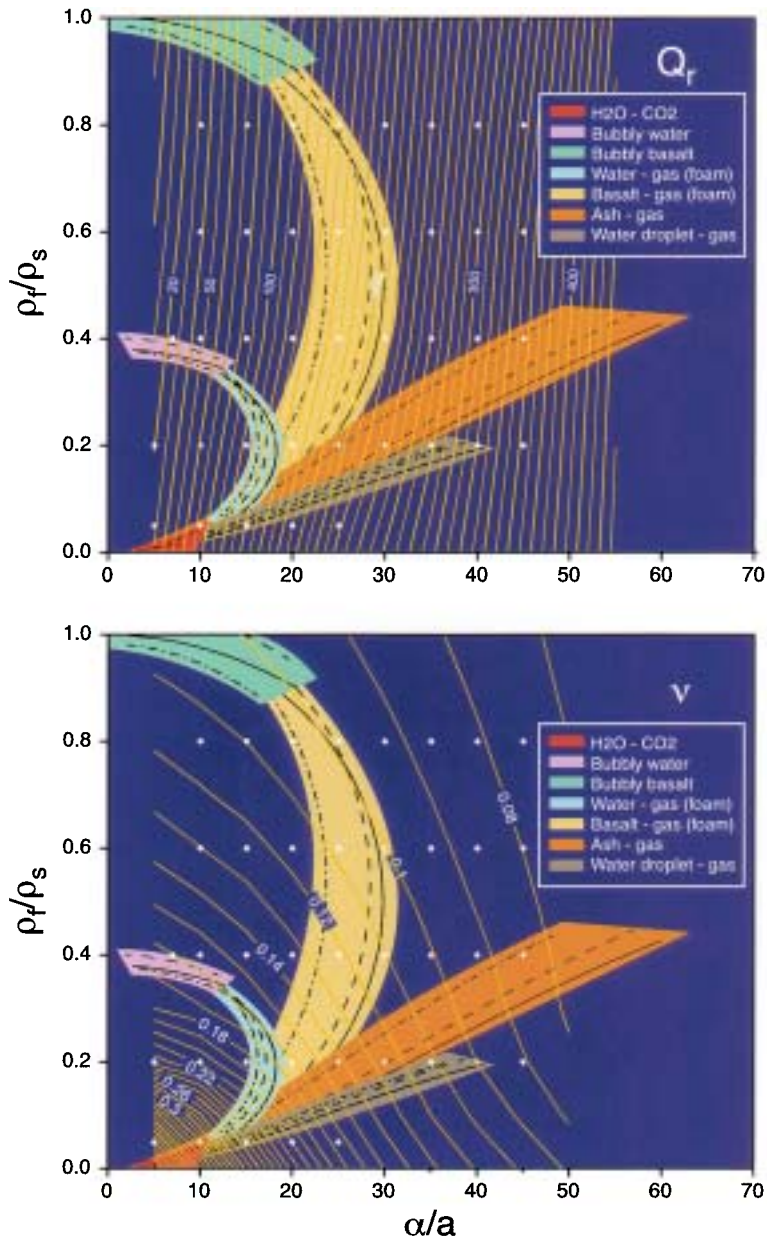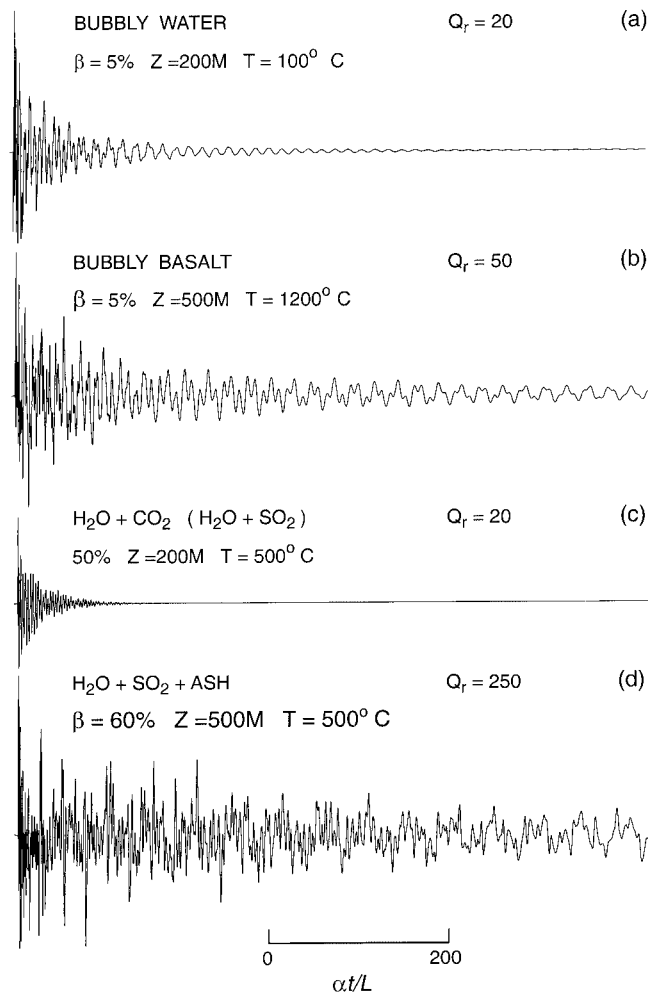
Figure 22

Synthetic far-field compressional waveforms produced by the excitation of a crack containing different types of fluids. The crack is embedded in a rock with fixed properties $\alpha = 2700\,\text{m/s}$, $\rho_s = 2500\,\text{kg/m}^3$. (a) Waveform for a crack at depth of 200 m containing bubbly water with 5% gas-volume fraction at a temperature of 100°C. (b) Waveform for a crack at depth of 500 m containing a bubbly basalt with 5% gas-volume fraction at a temperature of 1200°C. (c) Waveform for a crack at depth of 200 m containing a 50% mixture of either $H_2O - CO_2$ or $H_2O - SO_2$ gases at a temperature of 500°C. (d) Waveform for a crack a depth of 500 m containing an ash-laden gas with gas-volume fraction of 60% at a temperature of 500° C.

to several hundreds. KUMAGAI and CHOUET (2000) found that intrinsic absorption is trivial in gas-gas mixtures. No reliable estimates of Q_i are available for foams.

Figure 25 shows an example of application of the crack model to LP events recorded during a period of renewed activity at Kusatsu-Shirane Volcano, Japan.
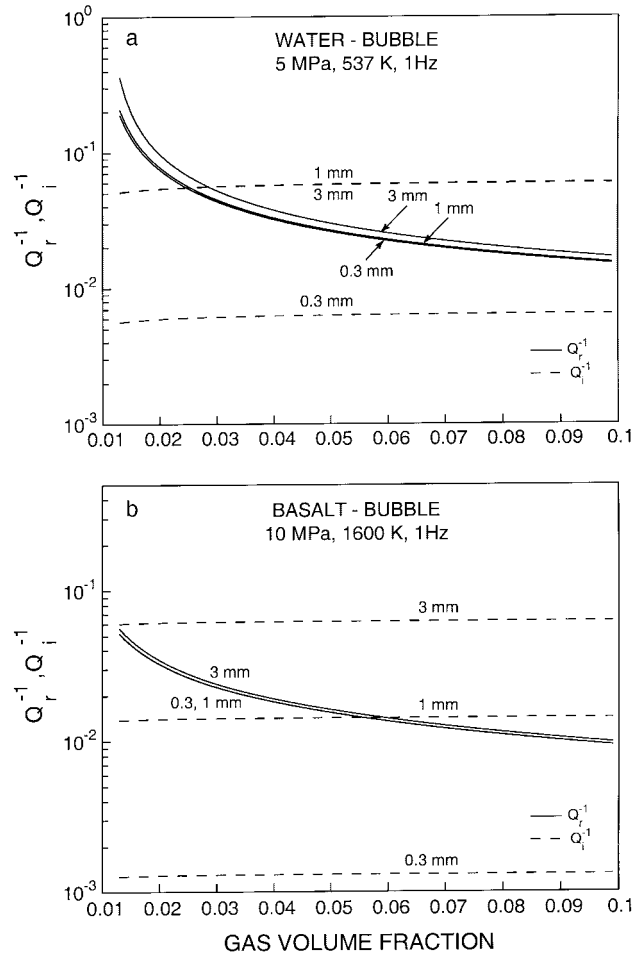
Figure 23

Comparison of Q_r^{-1} (solid lines) with Q_i^{-1} (dashed lines) for (a) bubbly water at 5 MPa and 537° K, and (b) bubbly basalt at 10 MPa and 1600° K as a function of gas-volume fraction for the three bubble radii 0.3, 1, and 3 mm, and frequency of the traveling wave of 1 Hz. (Reproduced from KUMAGAI and CHOUET, 2000.)

During this activity, LP events were frequently observed with hypocenters located several hundred meters below the summit crater (NAKANO *et al.*, 1998). High-quality records of this LP seismicity were obtained in September–November 1992 from a network of seismometers surrounding the source region (NAKANO *et al.*, 1998; KUMAGAI *et al.*, 2002; NAKANO *et al.*, 2002). The recorded events display a dominantly monochromatic signature (Fig. 18) with dominant frequency and factor Q both varying gradually with time (Fig. 25). Measurements of the dominant frequency and factor Q obtained by KUMAGAI *et al.* (2002) for individual events recorded over a 70-day period are shown together with fits obtained from the crack
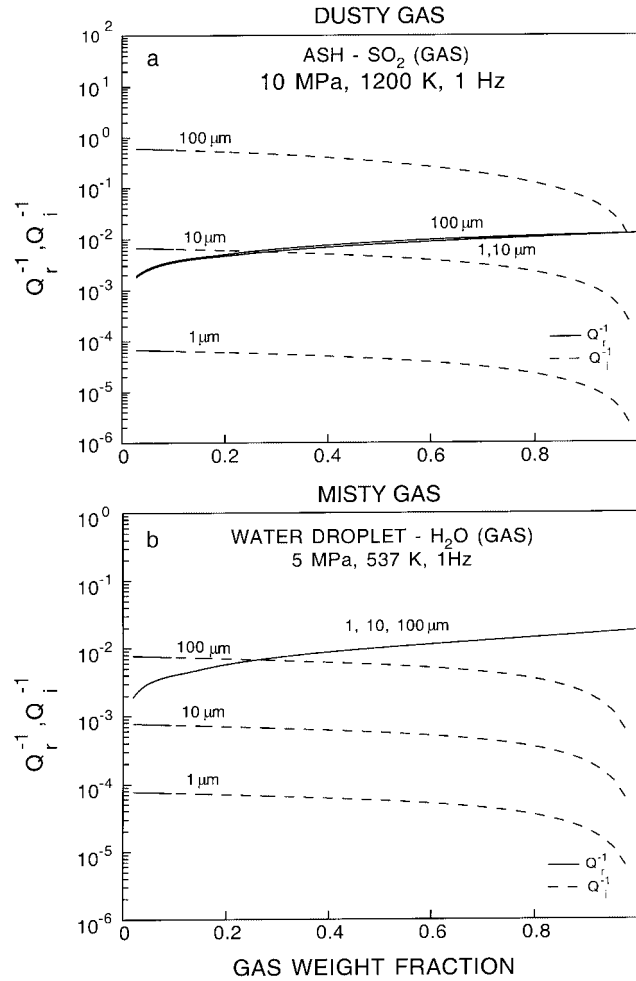
Figure 24

Comparison of Q_r^{-1} (solid lines) with Q_i^{-1} (dashed lines) for (a) ash-SO$_2$ gas mixture (dusty gas) at 10 MPa and 1200° K, and (b) water droplet-H$_2$O gas mixture (misty gas) at 5 MPa and 537° K for the three particle radii 1, 10, and 100 μm, and frequency of the traveling wave of 1 Hz. (Reproduced from KUMAGAI and CHOUET, 2000.)

model assuming that the fluid in the crack is a misty gas. The gas starts off fairly wet with 10% gas-weight fraction and ends up dry with 100% gas-weight fraction over the course of 70 days, suggesting a gradual heating of the LP source region. As the dominant mode of oscillation cannot be identified in these data, fits are obtained for different assumed modes. The fit in Figure 25a assumes that the mode $2W/5$ is the dominant mode and yields a crack length of 560 m. If one assumes instead that the dominant frequency represents the mode $2W/3$, one obtains essentially the same fit with a shorter crack length of 220 m (Fig. 25b).
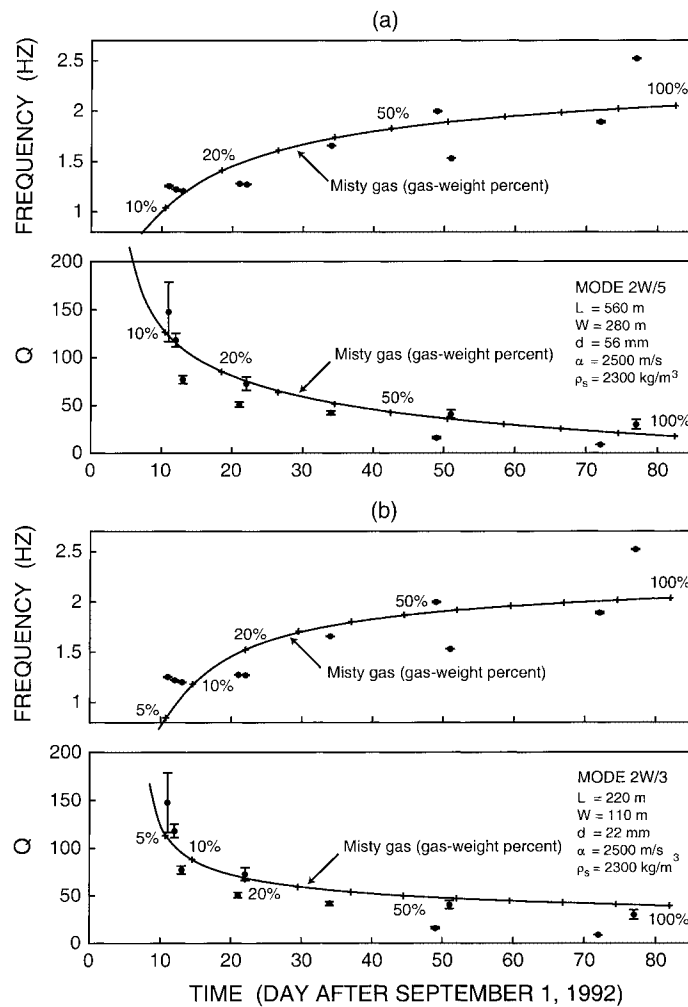
Figure 25

Temporal variation of Q and dominant frequency (solid dots with error bars) observed for LP events at Kusatsu-Shirane Volcano, Japan, in 1992. The solid line is the fit to these data obtained from the crack model assuming a crack filled with a misty gas. (a) Fit obtained assuming the observed dominant frequency represents the mode $2W/5$. (b) Fit obtained assuming the mode $2W/3$ dominates. (From KUMAGAI et al., 2002.)

Experimental Modelling of the Source Dynamics of Tremor

Although a good understanding of the resonance properties of resonators in the earth has been achieved, we still have a relatively poor understanding of the actual fluid dynamics and attendant pressure fluctuations underlying the excitation of LP events and tremor (JULIAN, 1994; CHOUET, 1996b; MORRISSEY and CHOUET, 1997). As

flows through volcanic conduits are not directly observable *in situ*, a useful approach to achieve a better understanding of such flows is to use analogue laboratory experiments. Expanding gas-liquid flows, designed to be analogous to those in volcanic conduits, were generated in the laboratory by LANE *et al.* (2001) using organic gas-gum rosin (natural pine resin) mixtures expanding in a narrow vertical tube of borosilicate glass connected to a vacuum chamber (Fig. 26). The tube is isolated from the vacuum chamber by a thin plastic diaphragm and an eruption is triggered by the rupture of the diaphragm. Depending on the level of volatile supersaturation, different flow regimes are observed, ranging from gentle unfragmented to violent fragmenting flows. The photograph in Figure 26 illustrates the growth of foam from the liquid interface and the unfragmented and fragmented regions of flow.

Figure 27 shows the pressure traces obtained at various heights in the tube during a fragmenting diethyl ether driven flow. Colors represent different flow regimes identified in video and still-camera images, and in optical and pressure sensor data. Figure 28 gives a schematic representation of the flow regimes and pressure oscillations in the fragmenting foam flow based on the positions of the flow regions 0.3 s into the flow (see Fig. 27). Region R4, shaded yellow, represents the source liquid. Region R3 in green shading, represents the foam growing from the surface of the source liquid. Region R2 in shades of pink and red, identifies a region where the foam becomes detached from the wall. This region is subdivided into a lower region R2b (pink in Fig. 28), in which gas pockets are developing at the wall, and an upper region R2a (red in Fig. 28) of gas-at-wall annular flow. Region 1, shaded blue, consists of foam fragments dispersed in gas. Region R1 is further subdivided into R1b (light blue in Fig. 28) and R1a (dark blue in Fig. 28) on the basis of the pressure oscillation behavior.

With the exception of R4, each region displays a characteristic pressure oscillation behavior (Fig. 27). Pressure oscillations are not detectable in R4 despite oscillations being present in the flow regions above this region. This implies that no oscillations are generated within the source liquid and also that no pressure disturbances can penetrate the liquid source region from the foam regions above. The reason for this probably lies in the strong impedance contrast between liquid and foam. This foam layer apparently acts like an acoustic barrier that prevents the pressure disturbances from propagating down into the source liquid.

Pressure oscillations in R3 display dominant frequencies in the range 10–30 Hz with pressure fluctuations $\Delta P/P$ of 2–10%, interpreted by LANE *et al.* (2001) as longitudinal oscillation modes of the foam column. Low-amplitude oscillations in the 80–100 Hz range are also present and may represent weak radial oscillation modes. A 50% increase in pressure oscillation amplitude is observed across the boundary from R3 to R2b. Pressure oscillations in region R2 have dominant frequencies of 10–30 Hz similar to those observed in region R3 and also show more prominent spectral peaks in the 80–100 Hz band. These oscillations were interpreted by LANE *et al.* (2001) to reflect both longitudinal and radial resonances in the detached section of the flow.
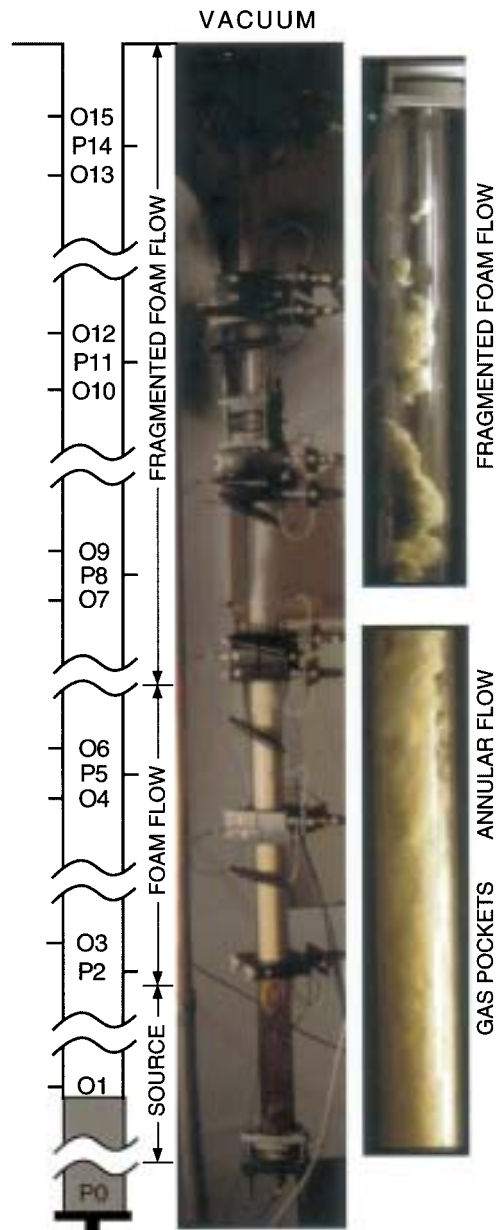
Figure 26

Experimental set up used by LANE *et al.* (2001) in their investigation of the dynamics of expanding gas-liquid flows. A 1.5-m-long tube with internal diameter of 3.8 cm is connected to a vacuum chamber with volume of $0.4\,m^3$. Optical (**O**) and pressure (**P**) transducers monitor the flow conditions along the tube. A still film camera image shows a fragmenting diethyl ether driven foam flow in progress, illustrating the growth of foam from the liquid interface and the unfragmented and fragmented regions of the flow. Digital video frames (1/400 s) show typical fragmented, gas-at-wall annular, and gas-pocket-at-wall regions of the flow. (Reproduced from LANE *et al.*, 2001.)
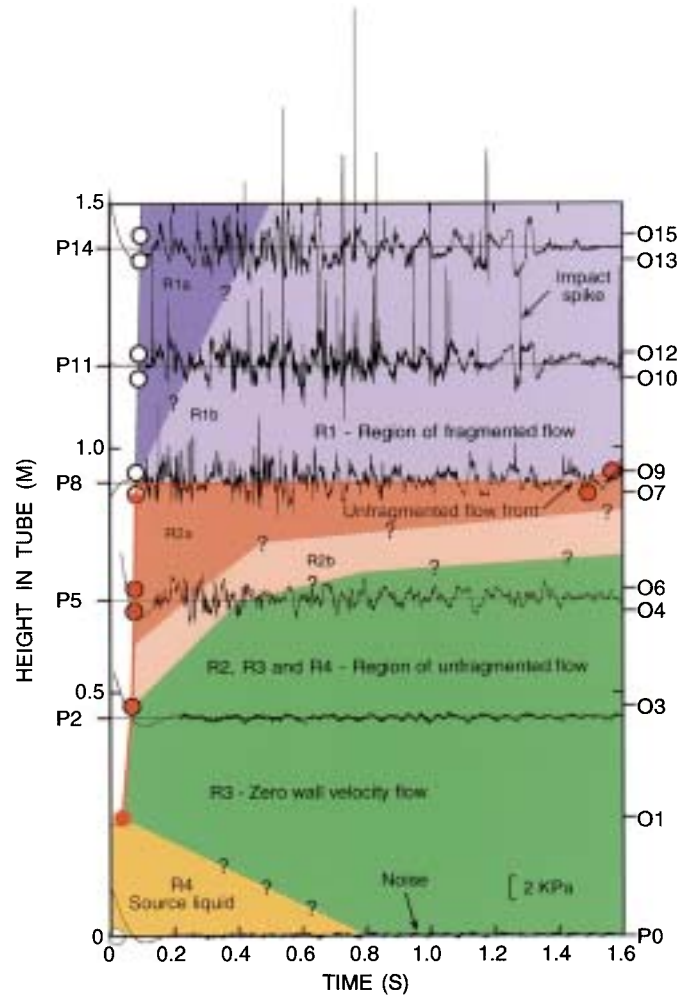
Figure 27
Height versus time plot of optical and pressure data for a fragmenting diethyl ether driven flow. The
positions of the pressure (**P**) and optical (**O**) transducers are indicated at the left and right, respectively.
Open circles mark the times at which the first 270 foam fragments are detected, and filled circles indicate
the onset of unfragmented flow. The circle at zero height represents the time at which **P14** detected pressure
falling below 99 kPa on decompression. The pressure data have been high-pass filtered at 5 Hz to remove
transducer drift. The noise-free section of pressure data between 0.1 and 0.3 s is synthetic data included to
reduce high-pass filter end effects. The pressure range (2 kPa) is indicated by the scale bar. Shading
identifies regions in which different flow regimes are observed (see text for details). (Reproduced from
LANE *et al*., 2001.)

Wave packets with frequencies in the range 0.5–5 kHz are commonly observed in
Regions R1b and R2a, rarely present in regions R1a and R2b, and never present in
regions R3 and R4. Thus, wave packets are dominantly present when the flow is fully
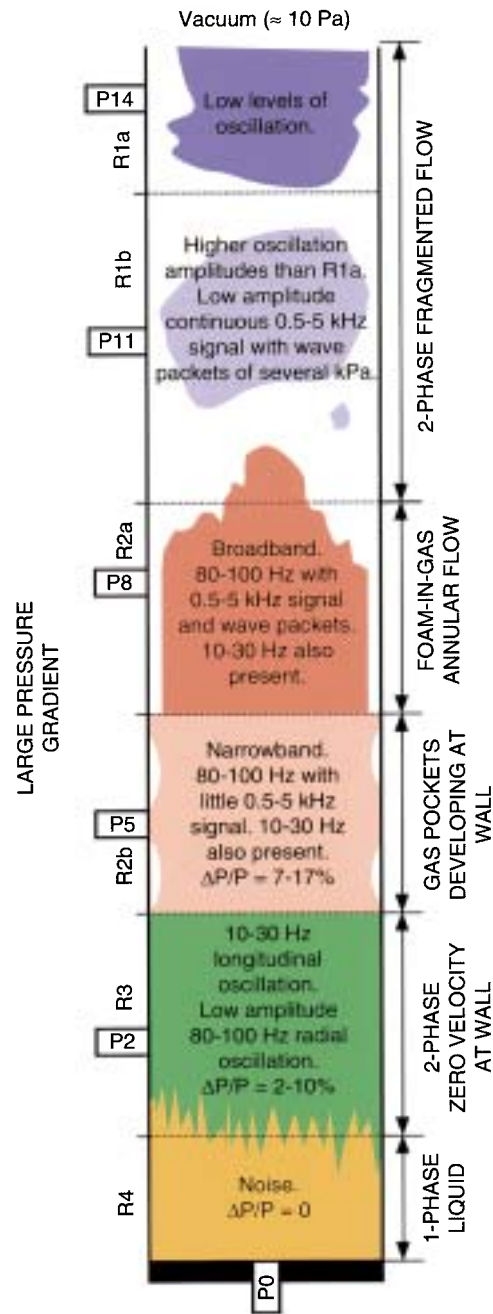
Figure 28

Schematic representation of flow regimes and pressure oscillations observed in a diethyl ether driven fragmenting foam flow. The positions of the pressure transducers are indicated at the left and the flow regions are representative of the conditions 0.3 s into the flow (see Fig. 27). (Reproduced from LANE *et al.*, 2001.)

detached from the tube wall but still interacting with the wall on occasion. Some wave packets have a broadband signature and represent impacts of gum rosin on the tube walls, while others display a spectrum encompassing a series of narrow-band peaks attributed to resonant oscillation of the gas between foam slugs. Region R1a is marked by low levels of oscillations.

Pressure oscillations were detected over the whole range of flow conditions explored by LANE *et al.* (2001), and spectral analyses of these oscillations indicated that the dominant oscillation frequencies could be attributed to resonant oscillations in both the foam and open gas spaces within the experimental tube. Flows in which foam fragmentation occurred displayed a broader, higher frequency and more energetic spectrum than unfragmented flows. Interestingly, some of the pressure data obtained by LANE *et al.* (2001) show remarkable similarities to LP and VLP data recorded for volcanoes. An example of such similarity is shown in Figure 29 which compares a vertical ground displacement record obtained at Kilauea with pressure pulses recorded during the diethyl ether driven flow near the point of optically detected fragmentation. The VLP events at Kilauea occurred during a transition from slow deflation to rapid inflation of the volcano. There are marked similarities between the two types of signals. Although the reasons for these similarities are not yet clear, they suggest that similar fluid mechanical processes may be operating in both laboratory experiments and in the fluids moving beneath Kilauea. Additional documentation of such similarities between laboratory and field observations is a prerequisite to translating seismic information into a refined understanding of volcanic flow processes and modeling those processes.

Conclusions

Volcano seismology provides a unique and powerful tool to study the dynamics of active magmatic and associated hydrothermal systems, determine the *in situ* mechanical properties of such systems, and interpret the nature, evolution and extent of magmatic energy source regions, all of which advance our understanding of eruptive behavior and enable the assessment of volcanic hazards. Three key questions summarize the situation with seismic observations regarding the nature and distribution of fluids and fluid mechanical processes beneath a volcano. These are: (1) can we distinguish different types of fluids by their LP signatures; (2) what are the excitation mechanisms of LP events and tremor; and (3) what is the geometry of the magma pathway? Answers to these questions might potentially contribute to improved prediction capability and improved scientific responses to volcanic crises to avert volcanic disasters, provided that the information can be obtained and applied in near real time (CHOUET, 1996a). The promise of a forecasting strategy based on LP seismicity is quite evident in its successful
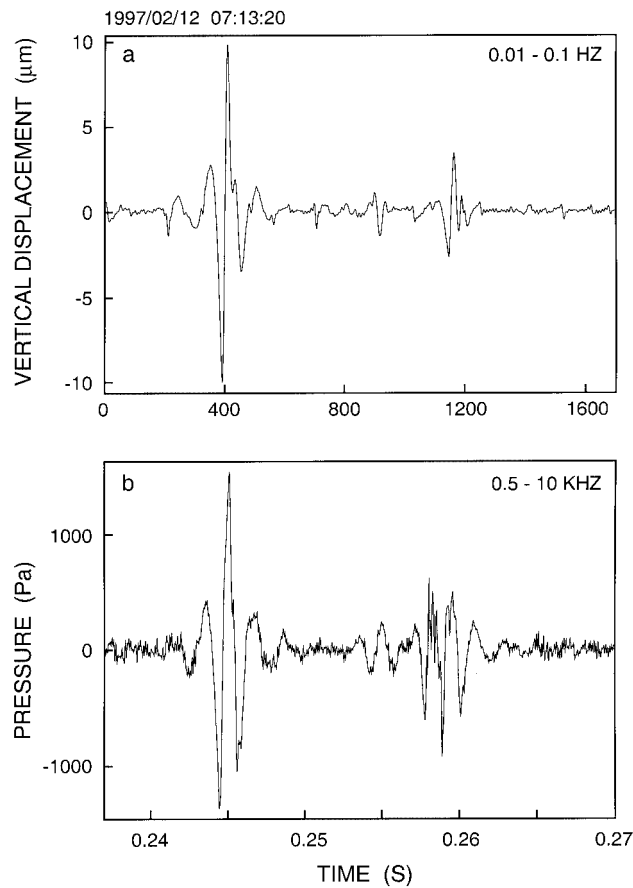
Figure 29

Comparison between (a) VLP displacement waveforms recorded at Kilauea Volcano on 12 February, 1997, during a transition from slow deflation to rapid inflation, and (b) pressure waveforms obtained at the boundary between regions R1 and R2 (see Figs. 27 and 28) in the diethyl ether driven fragmenting foam flow. The record in (a) has been band-pass filtered in the 0.01–0.1 Hz band, and the record in (b) has been similarly filtered in the 0.5–10 kHz band. Date and time at the start of the Kilauea record are indicated at the upper left. Notice the different time scales.

application to precursory swarms of LP events associated with the pressurization sequences leading to dome-destroying eruptions at Redoubt Volcano, Alaska (CHOUET et al., 1994; MORRISSEY and CHOUET, 1997), and its potential application to precursory LP events at volcanoes such as Galeras, Colombia (FISCHER et al., 1994; GIL CRUZ and CHOUET, 1997; STIX et al., 1997; NARVÁEZ et al., 1997), Soufriere Hills, Monserrat (WHITE et al., 1998), Popocatepetl, Mexico (ARCINIEGA-CEBALLOS et al., 2000), and Pinatubo, Philippines (WHITE et al., 1992; WHITE, 1996; RAMOS et al., 1999).

The acoustic properties of fluids may be inferred from the spectrum of LP seismicity. A caveat is that a crack containing different types of fluids can produce similar values of Q, so that interpretations of fluid types based on the observed Q may be manifold and equivocal. Uncertainties in intrinsic loss mechanisms and rock matrix properties and in the pressure and temperature conditions at the source of LP events further complicate the task of interpreting their source properties. Geological and geochemical constraints on possible fluid types beneath volcanoes are necessary to further constrain the seismological interpretation of LP events. In particular, further advances in real-time geochemical monitoring capabilities are needed to provide robust continuous data on volcanic fluids. Improvements in the resolution of 3-D velocity structures of volcanoes and improved locations for LP seismicity are also required to better fix the rock properties and thermodynamical conditions at the source. With additional constraints from geochemical and geological data, the spatial and temporal variations in the complex frequencies of LP events recorded on dense networks of seismometers offer great potential to image magmatic and hydrothermal systems beneath volcanoes.

As the resolution of the 3-D velocity structures of volcanoes sharpens, leading to more precise locations for LP events and improving the resolution of the forces operating at the source, the resolution of the source mechanisms of shallow LP events improves as well. Seismic source mechanisms, however, only yield clues about the fluid dynamics; thus, well-designed laboratory experiments simulating natural eruptive conditions, along with numerical modeling of such flows, are required for the identification of plausible fluid processes.

Although a direct link has been well established between shallow LP seismicity and eruptive activity, the relationship with deeper LP events is less clear. LP events are regularly observed at depths of 30–60 km beneath Kilauea, where their occurrence appears to be more directly related to deep magma supply dynamics than surface activity (AKI and KOYANAGI, 1981; SHAW and CHOUET, 1991). A low background of deep LP events is not uncommon, and may indeed be the rule rather than the exception as accumulating evidence now increasingly suggests (UKAWA and OHTAKE, 1987; HASEGAWA et al., 1991; PITT and HILL, 1994). The difficulty here has to do with our lack of knowledge concerning the character and dynamics of deep-seated fluid transport under volcanoes. The origin of deep LP seismicity still remains a major challenge to our understanding of eruptive phenomena.

Moment tensor inversions of VLP signals associated with variations in magma transport rate may be used to map the magma conduit structure (location, geometry, orientation, size) and to resolve the mass transport budget of magmatic fluids beneath a volcano. However, laboratory and numerical experiments of fluid mechanical processes analogous to those in volcanoes are again required to interpret flow processes compatible with the source mechanisms derived from seismic data.

Recent laboratory studies (LANE *et al.*, 2001) have elucidated self-excitation mechanisms inherent to fluid nonlinearity which are leading to a new understanding of the mechanisms underlying volcanic tremor. In parallel to these advances, numerical studies of multiphase flows are starting to shed light on both the micro- and macrophysics of these flows (e.g., VALENTINE and WOHLETZ, 1989; DOBRAN *et al.*, 1993), while new advances with computer models coupling the fluid dynamics with the elastodynamics in the solid (NISHIMURA and CHOUET, 1998) constitute the first steps toward a quantification of fluid processes in volcanoes and elastic radiation resulting from such processes. A comprehensive synthesis of seismic data derived by different methods such as discussed in this article, together with petrological, geochemical and geological data, and laboratory experiments, will be required to achieve a full understanding of the dynamics of active magmatic systems. Such endeavor is a prerequisite to accurate assessments of volcanic hazards and to mitigate the human and socio-economic loss from destructive eruptions.

Acknowledgements

REFERENCES

AKAIKE, H. (1974), *A New Look at the Statistical Model Identification*, IEEE Trans. Autom. Contr. *AC-9*, 716–723.

AKI, K. (1957), *Space and Time Spectra of Stationary Stochastic Waves, with Special Reference to Microtremors*, Bull. Earthquake Res. Inst. Tokyo Univ. *25*, 415–457.

AKI, K. (1959), *Correlational Study of Near Earthquake Waves*, Bull. Earthquake Res. Inst. Tokyo Univ. *37*, 207–232.

AKI, K. (1965), *A Note on the Use of Microseisms in Determining the Shallow Structures of the Earth's Crust*, Geophysics, *30*, 665–666.

AKI, K. (1977), *Three-dimensional Seismic Velocity Anomalies in the Lithosphere*, J. Geophys. *43*, 235–242.

AKI, K. (1984), *Evidence for Magma Intrusion during the Mammoth Lakes Earthquakes of May 1980 and Implications of the Absence of Volcanic (Harmonic) Tremor*, J. Geophys. Res. *89*, 7,689–7,696.

AKI, K. and LEE, W. H. K. (1976), *Determination of Three-dimensional Velocity Anomalies under a Seismic Array Using first P Arrival Times from Local Earthquakes, 1. A Homogeneous Initial Model*, J. Geophys. Res. *81*, 4,381–4,399.

AKI, K., CHRISTOFFERSSON, A., and HUSEBYE, E. S. (1976), *Three-dimensional Seismic Structure of Lithosphere under Montana LASA*, Bull. Seismol. Soc. Am. *66*, 501–524.

AKI, K., CHRISTOFFERSSON, A., and HUSEBYE, E. S. (1977a), *Determination of the Three-dimensional Seismic Structure of the Lithosphere*, J. Geophys. Res. *82*, 277–296.

AKI, K., FEHLER, M., and DAS, S. (1977b), *Source Mechanism of Volcanic Tremor: Fluid-driven Crack Models and their Application to the 1963 Kilauea Eruption*, J. Volcanol. Geotherm. Res. *2*, 259–287.

AKI, K., CHOUET, B., FEHLER, M., ZANDT, G., KOYANAGI, R., COLP, J., and HAY, R. G. (1978), *Seismic Properties of a Shallow Magma Reservoir in the Kilauea Iki by Active and Passive Experiments*, J. Geophys. Res. *83*, 2,273–2,282.

AKI, K. and KOYANAGI, R. (1981), *Deep Volcanic Tremor and Magma Ascent Mechanism under Kilauea, Hawaii*, J. Geophys. Res. *86*, 7,095–7,109.

ALMENDROS, J., CHOUET, B., and DAWSON, P. (2001a), *Spatial Extent of a Hydrothermal System at Kilauea Volcano, Hawaii, Determined from Array Analyses of Shallow Long-period Seismicity, 1: Method*, J. Geophys. Res. *106*, 13,565–13,580.

ALMENDROS, J., CHOUET, B., and DAWSON, P. (2001b), *Spatial Extent of a Hydrothermal System at Kilauea Volcano, Hawaii, Determined from Array Analyses of Shallow Long-period Seismicity, 2: Results*, J. Geophys. Res. *106*, 13,581–13,597.

ARCINIEGA-CEBALLOS, A., CHOUET, B. A., and DAWSON, P. (1999), *Very Long-period Signals Associated with Vulcanian Explosions at Popocatepetl Volcano, Mexico*, Geophys. Res. Lett. *26*, 3,013–3,016.

ARCINIEGA-CEBALLOS, A., VALDES-GONZALEZ, C., and DAWSON, P. (2000), *Temporal and Spectral Characteristics of Seismicity Observed at Popocatepetl Volcano, Central Mexico*, J. Volcanol. Geotherm. Res. *102*, 207–216.

BARTH, G. A., KLEINROCK, M. C., and HELZ, R. T. (1994), *The Magma Body at Kilauea Iki Lava Lake: Potential Insights into Mid-ocean Ridge Magma Chambers*, J. Geophys. Res. *99*, 7,199–7,217.

BENZ, H. M., CHOUET, B. A., DAWSON, P. B., LAHR, J. C., PAGE, R. A., and HOLE, J. A. (1996), *Three-dimensional P- and S-Wave Velocity Structure of Redoubt Volcano, Alaska*, J. Geophys. Res. *101*, 8,111–8,128.

BOUCHON, M. (1979), *Discrete Wave Number Representation of Elastic Wave Fields in Three-space Dimensions*, J. Geophys. Res. *84*, 3,609–3,614.

BOUCHON, M. (1981), *A Simple Method to Calculate Green's Functions for Elastic Layered Media*, Bull. Seismol. Soc. Am. *71*, 959–971.

CHOUET, B. (1979), *Sources of Seismic Events in the Cooling Lava Lake of Kilauea Iki, Hawaii*, J. Geophys. Res. *84*, 2,315–2,330.

CHOUET, B. (1981), *Ground Motion in the Near Field of a Fluid-driven Crack and its Interpretation in the Study of Shallow Volcanic Tremor*, J. Geophys. Res. *86*, 5,985–6,016.

CHOUET, B. (1982), *Free Surface Displacements in the Near Field of a Tensile Crack Expanding in Three Dimensions*, J. Geophys. Res. *87*, 3,868–3,872.

CHOUET, B. (1985), *Excitation of a Buried Magmatic Pipe: A Seismic Source Model for Volcanic Tremor*, J. Geophys. Res. *90*, 1,881–1,893.

CHOUET, B. (1986), *Dynamics of a Fluid-driven Crack in Three Dimensions by the Finite Difference Method*, J. Geophys. Res. *91*, 13,967–13,992.

CHOUET, B. (1987), *Representation of an Extended Seismic Source in a Propagator-based Formalism*, Bull. Seismol. Soc. Am. *77*, 14–27.

CHOUET, B. (1988), *Resonance of a Fluid-driven Crack: Radiation Properties and Implications for the Source of Long-period Events and Harmonic Tremor*, J. Geophys. Res. *93*, 4,375–4,400.

CHOUET, B., *A Seismic Model for the Source of Long-period Events and Harmonic Tremor*. In *Volcanic Seismology* (eds. P. Gasparini, R. Scarpa, and K. Aki) (Springer-Verlag, New York. 1992) pp. 133–156.

CHOUET, B. (1996a), *Long-Period Volcano Seismicity: Its Source and Use in Eruption Forecasting*, Nature *380*, 309–316.

CHOUET, B. (1996b), *New Methods and Future Trends in Seismological Volcano Monitoring*, In *Monitoring and Mitigation of Volcano Hazards*, (eds. R. Scarpa and R. Tilling) (Springer-Verlag, New York. 1996b) pp. 23–97.

CHOUET, B. A., PAGE, R. A., STEPHENS, C. D., LAHR, J. C., and POWER, J. A. (1994), *Precursory Swarms of Long-period Events at Redoubt Volcano (1989–1990), Alaska: Their Origin and Use as a Forecasting Tool*, J. Volcanol. Geotherm. Res. *62*, 95–135.

CHOUET, B., SACCOROTTI, G., MARTINI, M., DAWSON, P., DELUCA, G., MILANA, G., and SCARPA, R. (1997), *Source and Path Effects in the Wavefields of Tremor and Explosions at Stromboli Volcano, Italy*, J. Geophys. Res. *102*, 15,129–15,150.

CHOUET, B. A. and DAWSON, P. B. (1997), *Observations of Very-long-period Impulsive Signals Accompanying Summit Inflation of Kilauea Volcano, Hawaii, in February 1997*, EOS (Trans. Am. Geophys. Union), 78, no. 46 (Supplement), F429–F430.

CHOUET, B., DeLUCA, G., MILANA, G., DAWSON, P., MARTINI, M., and SCARPA, R. (1998), *Shallow Velocity Structure of Stromboli Volcano, Italy, Derived from Small-aperture Array Measurements of Strombolian Tremor*, Bull. Seismol. Soc. Am. 88, 653–666.

CHOUET, B., SACCOROTTI, G., DAWSON, P., MARTINI, M., SCARPA, R., DeLUCA, G., MILANA, G., and CATTANEO, M. (1999), *Broadband Measurements of the Sources of Explosions at Stromboli Volcano, Italy*, Geophys. Res. Lett. 26, 1,937–1,940.

COMMANDER, K. W. and PROSPERETTI, A. (1989), *Linear Pressure Waves in Bubbly Liquids: Comparison between Theory and Experiments*, J. Acoust. Soc. Am. 85, 732–746.

CROSSON, R. S. and BAME, D. A. (1985), *A Spherical Source Model for Low Frequency Volcanic Earthquakes*, J. Geophys. Res. 90, 10,237–10,247.

DAWSON, P. B., DIETEL, C., CHOUET, B. A., HONMA, K., OHMINATO, T., and OKUBO, P. (1998), *A Digitally Telemetered Broadband Seismic Network at Kilauea Volcano, Hawaii*, U.S. Geol. Surv. Open File Report 98–108, 1–121.

DAWSON. P. B., CHOUET, B. A., OKUBO, P. G., VILLASEÑOR, A., and BENZ, H. M. (1999), *Three-dimensional Velocity Structure of Kilauea Caldera, Hawaii*, Geophys. Res. Lett. 26, 2,805–2,808.

DOBRAN, F., NERI, A., and MACEDONIO, G. (1993), *Numerical Simulation of Collapsing Volcanic Columns*, J. Geophys. Res. 98, 4,231–4,259.

ELLSWORTH, W. L. and KOYANAGI, R. Y. (1977), *Three-dimensional Crust and Mantle Structure of Kilauea Volcano, Hawaii*, J. Geophys. Res. 82, 5,379–5,394.

FEHLER, M. (1983), *Observations of Volcanic Tremor at Mount St. Helens Volcano*, J. Geophys. Res. 88, 3,476–3,484.

FEHLER, M. and AKI, K. (1978), *Numerical Study of Diffraction of Plane Elastic Waves by a Finite Crack with Application to Location of a Magma Lens*, Bull. Seismol. Soc. Am. 68, 573–598.

FEHLER, M. and CHOUET, B. (1982), *Operation of a Digital Seismic Network on Mt. St. Helens Volcano and Observations of Long-period Seismic Events that Originate under the Volcano*, Geophys. Res. Lett. 9, 1,017–1,020.

FERRAZZINI, V. and AKI, K. (1987), *Slow Waves Trapped in a Fluid-filled Infinite Crack: Implication for Volcanic Tremor*, J. Geophys. Res. 92, 9,215–9,233.

FERRAZZINI, V., AKI, K., and CHOUET, B. (1991), *Characteristics of Seismic Waves Composing Hawaiian Volcanic Tremor and Gas-piston Events Observed by a Near-source Array*, J. Geophys. Res. 96, 6,199–6,209.

FISCHER, T. P., MORRISSEY, M. M., CALVACHE, M. L., GÓMEZ, V. D., TORRES, M. R., STIX, C. J., and WILLIAMS, S. N. (1994), *Correlations between SO_2 Flux and Long-period Seismicity at Galeras Volcano*, Nature, 368, 135–137.

FUJITA, E., IDA, Y., and OIKAWA, J. (1995), *Eigen Oscillation of a Fluid Sphere and Source Mechanism of Harmonic Volcanic Tremor*, J. Volcanol. Geotherm. Res. 69, 365–378.

FUJITA, E., FUKAO, Y., and KANJO, K. (2000), *Strain Offsets with Monotonous Damped Oscillations during the 1986 Izu-Oshima Volcano Eruption*, J. Geophys. Res. 105, 443–462.

GIL CRUZ, F. and CHOUET, B. A. (1997), *Long-period Events, the Most Characteristic Seismicity Accompanying the Emplacement and Extrusion of a Lava Dome in Galeras Volcano, Colombia, in 1991*, J. Volcanol. Geotherm. Res. 77, 121–158.

GOLDSTEIN, P. (1988), *Array Measurements of Earthquake Rupture*, Ph. D. Thesis, University of California Santa Barbara, Santa Barbara.

GOLDSTEIN, P. and ARCHULETA, R. J. (1987), *Array Analysis of Seismic Signals*, Geophys. Res. Lett. 14, 13–16.

GOLDSTEIN, P. and ARCHULETA, R. J. (1991a), *Deterministic Frequency-wavenumber Methods and Direct Measurements of Rupture Propagation during Earthquakes Using a Dense Array: Theory and Methods*, J. Geophys. Res. 96, 6,173–6,185.

GOLDSTEIN, P. and ARCHULETA, R. J. (1991b), *Deterministic Frequency-wavenumber Methods and Direct Measurements of Rupture Propagation during Earthquakes Using a Dense Array: Data Analysis*, J. Geophys. Res. 96, 6,187–6,198.

GOLDSTEIN, P. and CHOUET, B. (1994), *Array Measurements and Modeling of Sources of Shallow Volcanic Tremor at Kilauea Volcano, Hawaii*, J. Geophys. Res. *99*, 2,637–2,652.

HASEGAWA, A., ZHAO, D., HORI, S., YAMAMOTO, A., and HORIUCHI, S. (1991), *Deep Structure of the Northeastern Japan Arc and its Relationship to Seismic and Volcanic Activity*, Nature, *352*, 683–689.

HELZ, R. T. (1993), *Drilling Report and Core Logs for the 1988 Drilling of Kilauea Iki Lava Lake, Kilauea Volcano, Hawaii, with Summary Descriptions of the Occurrence of Foundered Crust and Fractures in the Drill Core*, U. S. Geological Survey Open-file Report 93-15, pp. 1–57.

HOLE, J. A. (1992), *Nonlinear High-resolution Three-dimensional Seismic Travel Time Tomography*, J. Geophys. Res. *97*, 6,553–6,562.

HUSEBYE, E. S., CHRISTOFFERSSON, A., AKI, K., and POWELL, C. (1976), *Preliminary Results on the Three-dimensional Seismic Structure of the Lithosphere under the USGS Central California Seismic Array*, Geophys. J. R. Astr. Soc. *46*, 319–340.

JULIAN, B. R. (1994), *Volcanic Tremor: Nonlinear Excitation by Fluid Flow*, J. Geophys. Res. *99*, 11,859–11,877.

KANAMORI, H., GIVEN, J. W., and LAY, T. (1984), *Analysis of Seismic Body Waves Excited by the Mount St. Helens Eruption of May 18, 1980*, J. Geophys. Res. *89*, 1,856–1,866.

KANESHIMA, S., KAWAKATSU, H., MATSUBAYASHI, H., SUDO, Y., TSUTSUI, T., OHMINATO, T., ITO, H., UHIRA, K., YAMASATO, H., OIKAWA, J., TAKEO, M., and IIDAKA, T. (1996), *Mechanism of Phreatic Eruptions at Aso Volcano Inferred from Near-field Broadband Seismic Observations*, Science, *273*, 642–645.

KAWAKATSU, H., OHMINATO, T., ITO, H., KUWAHARA, Y., KATO, T., TSURUGA, K., HONDA, S., and YOMOGIDA, K., (1992), *Broadband Seismic Observation at the Sakurajima Volcano, Japan*, Geophys. Res. Lett. *19*, 1,959–1,962.

KAWAKATSU, H., OHMINATO, T., and ITO, H. (1994), *10-s-period Volcanic Tremors Observed over a Wide Area in Southwestern Japan*, Geophys. Res. Lett. *21*, 1,963–1,966.

KAWAKATSU, H., KANESHIMA, S., MATSUBAYASHI, H., OHMINATO, T., SUDO, Y., TSUTSUI, T., UHIRA, K., YAMASATO, H., ITO, H., and LEGRAND, D. (2000), *Aso94: Aso Seismic Observation with Broadband Instruments*, J. Volcanol. Geotherm. Res. *101*, 129–154.

KIEFFER, S. W. (1977), *Sound Speed in Liquid-gas Mixtures: Water-air and Water-steam*, J. Geophys. Res. *82*, 2,895–2,904.

KUMAGAI, H. and CHOUET, B. A. (1999), *The Complex Frequencies of Long-period Seismic Events as Probes of Fluid Composition Beneath Volcanoes*, Geophys. J. Int. *138*, F7–F12.

KUMAGAI, H. and CHOUET, B. A. (2000), *Acoustic Properties of a Crack Containing Magmatic or Hydrothermal Fluids*, J. Geophys. Res. *105*, 25,493–25,512.

KUMAGAI, H., CHOUET, B. A., and NAKANO, M. (2002), *Temporal Evolution of a Hydrothermal System in Kusatsu-Shirane Volcano, Japan, Inferred from the Complex Frequencies of Long-period Events*, J. Geophys. Res., (in press).

KUMAZAWA, M., IMANISHI, Y., FUKAO, Y., FUROMOTO, M., and YAMAMOTO, A. (1990), *A Theory of Spectral Analysis Based on the Characteristic Property of a Linear Dynamic system*, Geophys. J. Int. *101*, 613–630.

LANE, S. J., CHOUET, B. A., PHILLIPS, J. C., DAWSON, P., RYAN, G. A., and HURST, E. (2001), *Experimental Observations of Pressure Oscillations and Flow Regimes in an Analogue Volcanic System*, J. Geophys. Res. *106*, 6,461–6,476.

LEGRAND, D., KANESHIMA, S., and H. KAWAKATSU (2000), *Moment Tensor Analysis of Broadband Waveforms Observed at Aso Volcano, Japan*, J. Volcanol. Geotherm. Res. *101*, 155–169.

MATSUBAYASHI, H. (1995), *The Source of the Long-period Tremors and the Very-long Period Events Preceding the Mud Eruption at Aso Volcano, Japan (in Japanese with English abstract)*, M. A. Thesis, Tokyo University, Tokyo.

MAVKO, G. M. (1980), *Velocity and Attenuation in Partially Molten Rocks*, J. Geophys. Res. *85*, 5,173–5,189.

MCNUTT, S. R. (2000a), *Volcanic Seismicity*. In *Encyclopedia of Volcanoes* (H. Sigurdsson, B. Houghton, S. R. McNutt, H. Rymer, and J. Stix eds.), pp. 1,015–1.033.

MCNUTT, S. R. (2000b), *Seismic Monitoring*. In *Encyclopedia of Volcanoes* (H. Sigurdsson, B. Houghton, S. R. McNutt, H. Rymer, and J. Stix eds.), pp. 1,095–1,119.

McNutt, S. R., Ida, Y., Chouet, B. A., Okubo, P., Oikawa, J., and Saccorotti, G. (1997), *Kilauea Volcano Provides Hot Seismic Data for Joint Japanese-U. S. Experiment*, EOS (Trans. Am. Geophys. Union), *78*, 105, 111.

Morrissey, M. M. and Chouet, B. A. (1997), *A Numerical Investigation of Choked Flow Dynamics and its Application to the Triggering Mechanism of Long-period Events at Redoubt Volcano, Alaska*, J. Geophys. Res. *102*, 7,965–7,983.

Morrissey, M. M. and Chouet, B. A. (2001), *Trends in Long-period Seismicity Related to Magmatic Fluid Compositions*, J. Volcanol. Geotherm. Res., *108*, 265–281.

Nakano, M., Kumagai, H., Kumazawa, M., Yamaoka, K., and Chouet, B. A. (1998), *The Excitation and Characteristic Frequency of the Long-period Volcanic event: An approach Based on an Inhomogeneous Autoregressive Model of a Linear Dynamic System*, J. Geophys. Res. *103*, 10,031–10,046.

Nakano, M., Kumagai, H., and Chouet, B. A. (2002), *Source Mechanism of Long-period Events at Kusatsu-Shirane Volcano, Japan, Inferred from Waveform Inversion of the Effective Excitation Functions*, J. Volcanol. Geotherm. Res., submitted.

Narváez, M. L., Torres, R. A., Gómez., C. D. M., Cortés, G. P. Cepeda, J. H., and Stix, J. (1997), *'Tornillo'-type Seismic Signals at Galeras Volcano, Colombia, 1992–1993*, J. Volcanol. Geotherm. Res. *77*, 159–171.

Neuberg, J., Luckett, R., Ripepe, M., and Braun, T., (1994), *Highlights from a Seismic Broadband Array on Stromboli Volcano*, Geophys. Res. Lett. *21*, 749–752.

Nishimura, T., Nakamichi, H., Tanaka, S., Sato, M., Kobayashi, T., Ueki, S., Hamaguchi, H., Ohtake, M., and Sato, H. (2000), *Source Process of Very Long Period Seismic Events Associated with the 1998 Activity of Iwate Volcano, Northeastern Japan*, J. Geophys. Res. *105*, 19,135–19,147.

Nishimura, T. and Chouet, B. (1998), *Numerical Simulations of Seismic Waves and Magma Dynamics Excited by a Volcanic Eruption*, EOS (Trans. Am. Geophys. Union) *79*, no. 45 (Supplement), F595.

Ohminato, T. and Chouet, B. A. (1997), *A Free-surface Boundary Condition for Including 3D Topography in the Finite Difference Method*, Bull. Seismol. Soc. Am. *87*, 494–515.

Ohminato, T. and Ereditato, D. (1997), *Broadband Seismic Observations at Satsuma-Iwojima Volcano, Japan*, Geophys. Res. Lett. *24*, 2,845–2,848.

Ohminato, T., Chouet, B. A., Dawson, P. B., and Kedar, S. (1998), *Waveform Inversion of Very-long-period Impulsive Signals Associated with Magmatic Injection beneath Kilauea Volcano, Hawaii*, J. Geophys. Res. *103*, 23,839–23,862.

Okubo, P. G., Benz, H. M., and Chouet, B. A. (1997), *Imaging the Crustal Magma Source beneath Mauna Loa and Kilauea Volcanoes, Hawaii*, Geology *25*, 867–870.

Pitt, A. M. and Hill, D. P. (1994), *Long-period Earthquakes in the Long Valley Caldera Region, Eastern California*, Geophys. Res. Lett. *21*, 1,679–1,682.

Podvin, P. and Lecomte, I. (1991), *Finite Difference Computation of Traveltimes in Very Contrasted Velocity Models: A Massively Parallel Approach and its Associated Tools*, Geophys. J. Int. *105*, 271–284.

Ramos, E. G., Hamburger, M. W., Pavlis, G. L., and Laguerta E. P. (1999), *The Low-frequency Earthquake Swarms at Mount Pinatubo, Philippines: Implications for Magma Dynamics*, J. Volcanol. Geotherm. Res. *92*, 295–320.

Richter, D. H. and Moore, J. G. (1966), *Petrology of the Kilauea Iki Lava Lake, Hawaii*, U. S. Geological Survey Professional Paper 537-B, pp. B1–B26.

Richter, D. H., Eaton, J. P., Murata, K. J., Ault, W. U., and Krivoy, H. L., (1970), *Chronological Narative of the 1959–60 eruption of Kilauea Volcano, Hawaii*, U. S. Geological Survey Professional Paper 537-E, pp. E1–E73.

Rowan, L. R. and Clayton, R. W. (1993), *The Three-dimensional Structure of Kilauea Volcano, Hawaii, from Travel-time Tomography*, J. Geophys. Res. *98*, 4,355–4,375.

Rowe, C. A., Aster, R. C., Kyle, P. R., Schlue, J. W., and Dibble, R. R. (1998), *Broadband Recording of Strombolian Explosions and Associated Very-long-period Seismic Signals on Mount Erebus Volcano, Ross Island, Antarctica*, Geophys. Res. Lett. *25*, 2,297–2,300.

Scarpa, R. and Tilling, R. I., *Monitoring and Mitigation of Volcano Hazards*, (Springer-Verlag, New York (1996)), 841 pp.

Schmidt, R. O. (1981), *A Signal Subspace Approach to Multiple Emitter Location and Spectral Estimation*, Ph. D. Thesis, Stanford University, Palo Alto.

SCHMIDT, R. O. (1986), *Multiple Emitter Location and Signal Parameter Estimation*, IEEE Trans. Antennas Propagation, *34*, 276–280.

SHAW, H. R. and CHOUET, B. (1991), *Fractal Hierarchies of Magma Transport in Hawaii and Critical Self-organization of Tremor*, J. Geophys. Res. *96*, 10,191–10,207.

SPUDICH, P. and OPPENHEIMER, D. (1986), *Dense Seismograph Array Observations of Earthquake Rupture Dynamics*. In *Earthquake Source Mechanics*, Geophys. Monogr. Ser. *37*, (eds. S. Das, J. Boatwright and C. D. Scholz), 285–296, AGU, Washington.

STIX, J., TORRES, R., NARVÁEZ, C. L., CORTÉS, M. G. P., RAIGOSA, J. J., GÓMEZ, A. D. and CASTONGUAY, R. (1997), *A Model of Vulcanian Eruptions at Galeras Volcano, Colombia*, J. Volcanol. Geotherm. Res. *77*, 285–303.

TAKEI, Y. and KUMAZAWA, M. (1994), *Why Have the Single Force and Torque been Excluded from Seismic Source Models?* Geophys. J. Int. *118*, 20–30.

TAKEI, Y. (1998), *Constitutive Mechanical Relations of Solid-liquid Composites in Terms of Grain-boundary Contiguity*, J. Geophys. Res. *103*, 18,183–18,203.

TEMKIN, S. and DOBBINS, R. A. (1966), *Attenuation and Dispersion of Sound by Particulate-relaxation Processes*, J. Acoust. Soc. Am. *40*, 317–324.

THORNBER, C. R., HELIKER, C. C., REYNOLDS, J. R., KAUAHIKAUA, J., OKUBO, P., LISOWSKI, M., SUTTON, A. J., and CLAGUE, D. (1996), *The Eruptive Surge of February 1, 1996: A Highlight of Kilauea's Ongoing East Rift Zone eruption*, EOS (Trans. Am. Geophys. Union), *77*, no. 46 (Supplement), F798.

THURBER, C. H. (1984), *Seismic Detection of the Summit Magma Complex of Kilauea Volcano, Hawaii*, Science, *223*, 165–167.

THURBER, C. H. (1987), *Seismic Structure and Tectonics of Kilauea Volcano*, U. S. Geological Survey Professional Paper *1350*, 919–934.

UKAWA, M. and OHTAKE, M. (1987), *A Monochromatic Earthquake Suggesting Deep-seated Magmatic Activity Beneath the Izu-Ooshima Volcano, Japan*, J. Geophys. Res. *92*, 12,649–12,663.

VALENTINE, G. A. and WOHLETZ, K. H. (1989), *Numerical Models of Plinian Eruption Columns and Pyroclastic Flows*, J. Geophys. Res. *94*, 1,867–1,887.

VIDALE, J. (1988), *Finite-difference Calculations of Traveltimes*, Bull. Seismol. Soc. Am. *78*, 2,062–2,076.

VIDALE, J. (1991), *Finite-difference Calculation of Traveltimes in Three Dimensions*, Geophysics, *55*, 521–526.

WALLIS, G. B., *One-Dimensional Two-Phase Flow*, McGraw-Hill, New York. (1969), 408 pp,.

WHITE, R. A. (1996), *Precursory Deep Long-period Earthquakes at Mount Pinatubo, Philippines: Spatio-temporal Link to a Basalt Trigger*. In *Fire and Mud: Eruptions and Lahars of Mount Pinatubo, Philippines*, (Newhall, C., and Punongbayan, R., eds.), PHIVOLCS and Univ. Washington Press, pp. 307–328.

WHITE, R., HARLOW, D., and CHOUET, B. (1992), *Long-period Earthquakes Preceding and Accompanying the June 1991 Mount Pinatubo Eruptions*, EOS (Trans. Am. Geophys. Union) *73*, no. 43 (Supplement), 347.

WHITE, R. A., MILLER, A. D., LYNCH, L., and POWER, J., (1998), *Observations of Hybrid Seismic Events at Soufriere Hills Volcano, Montserrat: July 1995 to September 1996*, Geophys. Res. Lett. *25*, 3,657–3,660.

To access this journal online:
http://www.birkhauser.ch